PHASE CHANGES AND TRANSPORT PROPERTIES OF GEOPHYSICAL MATERIALS UNDER SHOCK LOADING

Thesis by

Kathleen Gabrielle Holland

In Partial Fulfillment of the Requirements

for the degree of

Doctor of Philosophy

California Institute of Technology

Pasadena, California

1997

(submitted May 29, 1997)

Acknowledgments.

I thank my advisor, Dr. Thomas J. Ahrens for his helpful advice, timely manuscript revisions, and the use of his one-of-a-kind laboratory.

I thank my thesis committee, Dr. Joann Stock, Dr. David Stevenson, Dr. Peter Wyllie, and Dr. Michael Gurnis for their helpful comments and suggestions on the manuscript.

I thank my husband Jacob E. Holland, for his love and support, and for always being there when I needed him. I also thank him for aiding me in writing some of the programs that I used to reduce my data. I thank my parents, Suellen R. Gallagher and Jerrold E. Gallagher for their emotional as well as financial support.

This research was supported by NSF grant EAR 92-19906 (Ahrens), EAR 95-06377 (Ahrens) and DMR 92-02587 (Atwater). I am grateful to Dr. Raymond Jeanloz and Dr. Michael Manga for technical discussions, Dr. Shijie Zhong for assistance with numerical calculations, and to Dr. Neil Holmes, Dr. Stanley Love and Dr. Jessica Faust for helpful comments on the manuscripts, as well as to Michael Long, Epaprodito Gelle, Alberto Devora and Paul Carpenter for experimental assistance. I thank Dr. Harry Atwater and Dr. Imran Hashim for use of the argon ion sputtering apparatus and for invaluable aid in making my thin iron films, Reynold Johnson, Dr. Axel Scherer and Chuan-Cheng Cheng for the use of and assistance with the evaporative coaters that I used to apply silver coatings to my samples, and Dr. George Rossman for the use of his optical multi-channel analyzer.

Abstract

Kathleen Gabrielle Holland, Ph.D.

California Institute of Technology, 1997

The lower mantle of the Earth is believed to be largely composed of $(Mg, Fe)O$ (magnesiowüstite) and $(Mg, Fe)SiO_3$ (perovskite); thus the high pressure phase of $(Mg, Fe)_2SiO_4$ (olivine), which is believed to be perovskite plus magnesiowüstite is of geophysical interest. Radiative temperatures of single-crystal olivine starting material $[(Mg_{0.9}, Fe_{0.1})_2SiO_4]$ decreased abruptly from 7040±315 to 4300±270 K upon shock compression above 80 GPa. The data indicate that an upper bound to the solidus of the magnesiowüstite and perovskite assemblage at 4300 ± 270 K is 130 ± 3 GPa. These conditions correspond to those for partial melting at the base of the mantle, as has been suggested to occur within the recently discovered ultra-low-velocity zone (ULVZ) beneath the Central Pacific. We construct speculative high pressure phase diagrams for the MgO – SiO_2 system using experimental data from our work, and other mineral physics experiments.

In separate experiments, time dependent shock temperatures were measured for stainless steel (SS) films sandwiched between two transparent Al_2O_3 anvils. The anvil material was the same as the driver material so that there would be symmetric heat flow from the sample. Inferred Hugoniot temperatures, T_h, of 5000 - 8500±500 K at 222

- 321 GPa are consistent with previous measurements in SS. Temperatures at the film–anvil interface (T_i), which are directly measured (rather than T_h) indicate that T_i did not decrease measurably during the approximately 250 ns that the shock wave took to traverse the Al_2O_3 anvil. Thus an upper bound is obtained for the thermal diffusivity of Al_2O_3 at the metal/anvil interface of $\kappa \leq 14 \pm 5$ cm$^2/s$ at 208 GPa and 2110 K. This is a factor of 1.6 lower than previously calculated values, resulting in a decrease of the inferred T_h by at least 400 K. The observed shock temperatures are combined with temperatures calculated from measured Hugoniots and are used to calculate the thermal conductivity of Al_2O_3. There was no measurable radiant-intensity decrease during the time when the shock wave propagated through the anvil; we infer from this that Al_2O_3 remained transparent while in the shocked state. Thus an Al_2O_3 anvil is sufficiently transparent for shock temperature measurements for metals, to at least 240 GPa.

Finally, shock temperature experiments employing a six-channel pyrometer were conducted on 200, 500, and 1000 Å thick films of Fe sandwiched between 3 mm thick anvils of Al_2O_3 and LiF, to measure the thermal diffusivity ratios of Al_2O_3/Fe and LiF/Fe, at high temperatures and pressures. Temperature decays of 3000 ± 800 K in 250 ns were observed at Fe pressures of 194 - 303 GPa, which reflect the conduction of heat from the thin metal films into the anvil material. These results were achieved in experiments employing LiF anvils at 164 - 166 GPa and 4190 - 4220 K, and Al_2O_3 anvils at 196 - 303 GPa and 1410 - 2750 K. Thermal modeling of interface temperature versus time yields best fit thermal diffusivity ratios ranging from 15 ± 30 to 80 ± 20 (Fe/anvil) over the pressure and temperature range of the experiments. Calculated thermal conductivities for Fe, using electron gas theory, of 110 – 212 W/mK are used to calculate thermal conductivities for the anvil materials ranging from 6 to 12 W/mK. Debye theory predicts higher values of 8 to 34 W/mK. Data from previous experiments on thick ($\geq 100\mu$m) films of Fe and stainless steel are combined with our present results from experiments on thin ($\leq$ 1000 Å) films to infer a 5860 ± 390 K Hugoniot temper-

ature for the onset of melting of iron at 243 GPa. Our results address the question of whether radiation observed in shock temperature experiments on metals originates from the metal at the metal/anvil interface or from the shocked anvil. We conclude that the photon flux from the shocked iron/anvil sandwich recorded in all experiments originates from the metal. Within the uncertainties of the shock temperature data, the uncertainties in shock temperatures resulting from the radiation from the anvils is negligible. This is in direct disagreement with previous conclusions of Kondo.

Contents

List of Figures

List of Tables

Introduction

Outline of Thesis

This thesis consists of four chapters and one appendix. The first three chapters are adapted from papers. A more concise version of Chapter 1 appeared in *Science* [Holland and Ahrens, 1997]; an earlier version of Chapter 2 appeared in a proceedings volume of an AIRAPT conference [Gallagher et al., 1994]; and Chapter 3 appeared in the proceedings volume of the Joint U.S. - Japan Seminar on High Pressure, January 1996 [Holland and Ahrens, 1998]. The appendix is an unpublished report, which contains technical details about the numerical modeling of the thin-film experiments. Because some of the chapters were originally meant to stand alone, there is some redundancy of material between the second and third chapters.

Summary

Garnero and Helmberger [1995] discovered that there is a distinct drop in seismic P-wave velocity within 40 km of the core-mantle boundary (CMB), called the ultra-low-velocity-zone (ULVZ). Williams and Garnero [1996] interpreted the ULVZ as a partial melt at the base of the mantle. Thus, shock wave experiments that constrain the high pressure melting temperature of the high pressure assemblage of $(Mg,Fe)_2SiO_4$ olivine (MgO + $MgSiO_3$) are of great geophysical interest. In Chapter 1, the results of a series of shock

temperature experiments on olivine are reported. A major objective is to determine the shock temperature at which the Hugoniot of the high pressure assemblage of olivine ($MgO + MgSiO_3$) crosses the phase boundary that is believed to represent melting, and thus determine a 4300 $\pm$ 270 K upper bound to the solidus temperature of the high pressure assemblage. If the ULVZ does in fact represent partial melt, then our experiments may constrain the temperature at the top of the core to be $\leq$ 4300 K.

Another constraint on temperatures within the deep Earth can be obtained by studying phase changes in iron. The Earth's inner-core/outer-core boundary temperature is constrained by the temperature of the transition from liquid to solid iron. However the density of the core is not consistent with pure iron; there is believed to be a light alloying element or elements that reduces the density of the outer core by 10% from pure iron [Birch , 1952], and of the inner core by 3–7% [Jephcoat and Olson, 1987]. Shock temperatures of iron alloys, such as 304 stainless steel, are of interest because they provide data showing the difference in the melting temperature between pure iron and iron alloys of 700 $\pm$ 30 K at 243 GPa. This agrees well with data by Boehler [1992] and by Anderson and Ahrens [1996] showing that iron alloys have a depressed melting point, for instance, the melting temperature of mixtures of Fe and FeS are $\sim$ 600 K less than that of pure Fe at 136 GPa [Boehler, 1992].

Shock temperatures of iron and iron alloys are used to constrain the temperature at the inner core boundary (ICB) of the Earth. In chapter 2, measurements are reported of the shock temperatures of 304 stainless steel and a new target configuration is described for constraining high-pressure steel/Al_2O_3 diffusivity ratios, which are important in reducing shock temperature data. With this new target configuration, a lack of measurable thermal decay of interface temperature is reported. This places a constraint on the thermal diffusivity of Al_2O_3 of 14 $\pm$ 5 cm^2/s at 208 GPa.

In chapter 3, the decrease with time of Fe/Al_2O_3 and Fe/LiF interface temperatures are reported which are caused by heat flow from the high-temperature, high-pressure Fe

films into the surrounding high-pressure transparent anvil materials. Thermal diffusivity ratios of 70 to 80 for Fe/Al_2O_3 are reported in the 160 to 250 GPa anvil pressure range. This result is up to a factor of 2 lower than calculated with Debye theory (for the anvil materials) and free electron gas theory (for the iron). Also Fe/LiF ratios of 15 to 35 were obtained at 165 GPa, a factor of 0.8 to 1.2 lower than calculated from Debye and free electron gas theory. This may be, in part, explained by the observation that Debye theory is only a first approximation (for example, it overestimates the heat capacity of calcite at ambient conditions by 33% [Yang, 1996]).

Chapter 1

Melting of $(Mg, Fe)_2SiO_4$ in the core-mantle boundary of the Earth

1.1 Silicate Fusion

The major minerals of Earth's lower mantle are thought to be $(Mg_{0.94}, Fe_{0.06})SiO_3$ perovskite, Pv, and $(Mg_{0.84}, Fe_{0.16})O$ magnesiowüstite, Mw, whose magnesium end-member is periclase, Pc [Allègre et al., 1995; Weidner, 1986; Stixrude et al., 1992; Jeanloz and Morris, 1986]. Thus, the melting behavior of this assemblage is important for determining both the temperature of the mantle, and the origin of seismically imaged structures at the core-mantle boundary (CMB). Very extensive work on Twin Sisters dunite [McQueen et al., 1967] consisting largely of olivine with composition of $(Mg_{0.9}, Fe_{0.1})_2SiO_4$ and hot pressed synthetic forsterite (Mg_2SiO_4) demonstrated that the olivine structure begins to transform into a high pressure assemblage starting at approximately 30 GPa along the Hugoniot. This is marked by the onset of a mixed

phase region as shown in Figure 1.1.

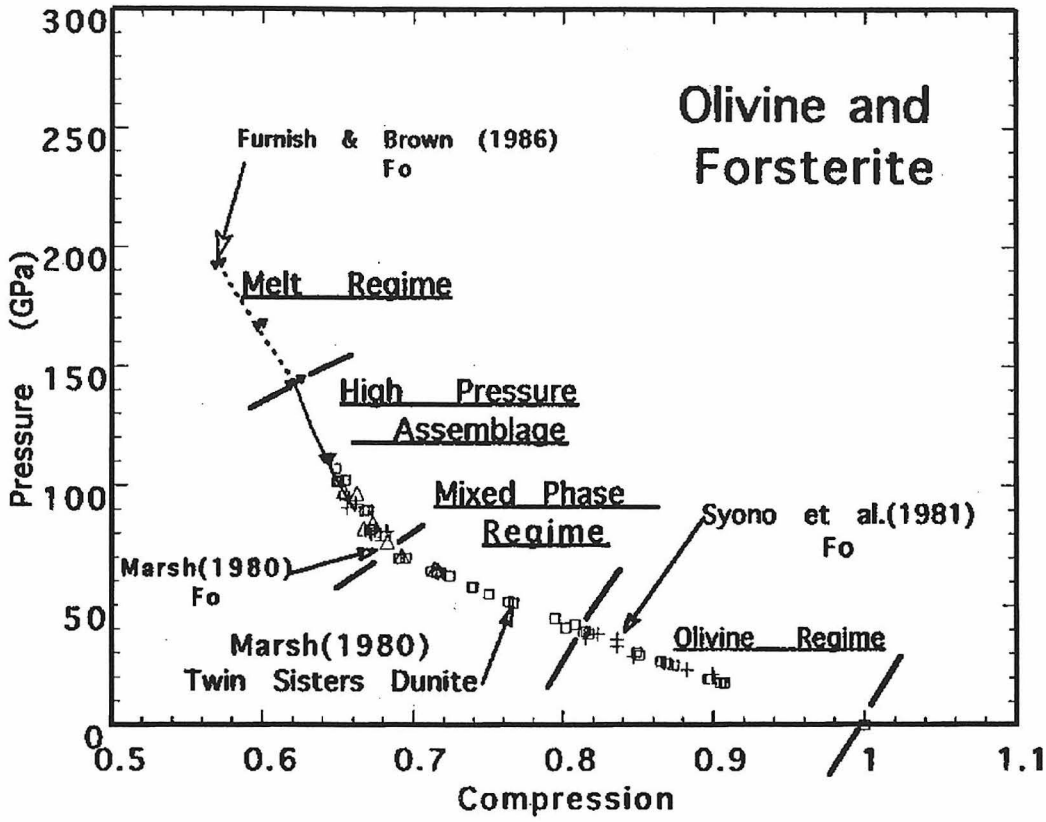

Figure 1.1: Pressure-compression (P/ρ) for Twin Sisters dunite [Marsh, 1980; McQueen et al., 1967; Syono et al., 1981] and forsterite and peridot [Furnish and Brown, 1986]. Different regimes along the Hugoniot are shown.

Recent studies of the solidus of perovskite are disparate: the melting temperatures of pure $MgSiO_3$ perovskite at 130 GPa (the pressure of the CMB) have been estimated at 7800 $\pm$ 800 K [Zerr and Boehler, 1993] and 4500$\pm$350 K [Knittle and Jeanloz, 1989; Heinz et al., 1994]. These perovskite melting temperatures were measured up to 60, 96 and 60 GPa, respectively and extrapolated to 130 GPa. Measurements of the melting of Pc taken at pressures up to 31.5 GPa result in 4000 $\pm$ 200 K [Zerr and Boehler, 1994]. When extrapolated to 130 GPa, they imply that periclase melts at 5100$\pm$750 K. Phase equilibrium experiments [Davis and England, 1964; Gasparik, 1990; Presnall

and Walter, 1993; Presnall, 1995] demonstrate that at lower mantle pressures the stable high-pressure phase (hpp) assemblage for Mg_2SiO_4 forsterite, Fo, is Pc + Pv; thus Fo can be used as a representative starting material in shock experiments (Figure 1.2). Note that above 22 GPa, Pc + Pv melt to Pc + liquid rather than Pv + liquid. Syono

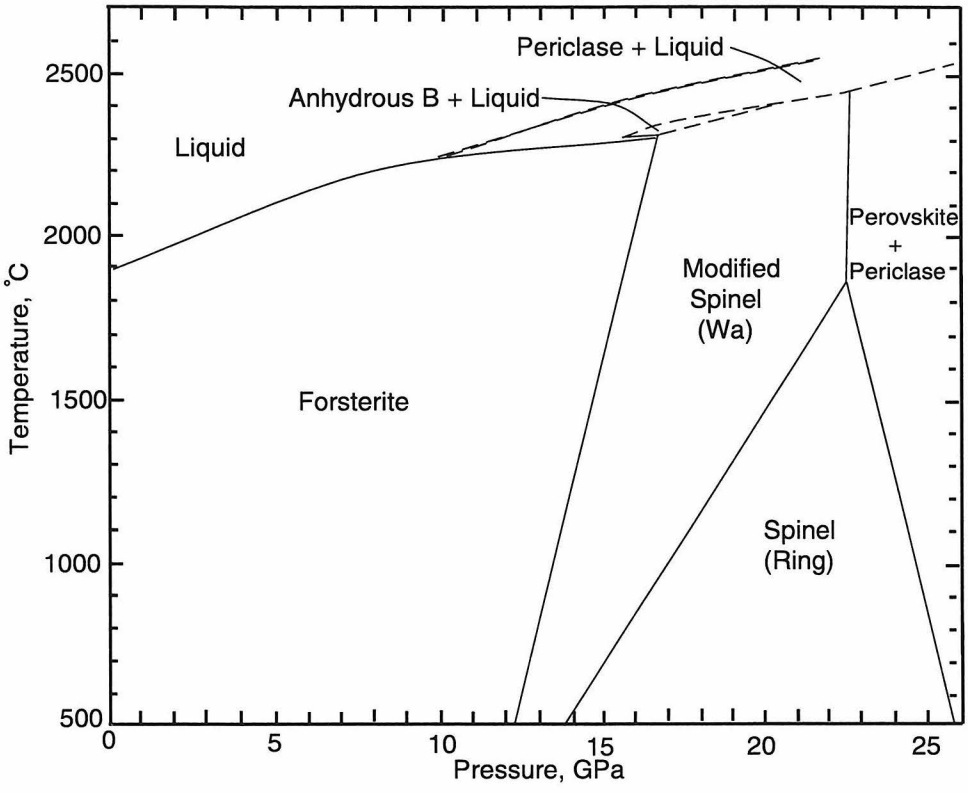

Figure 1.2: Phase diagram for the composition Mg_2SiO_4 to 26 GPa [Davis and England, 1964; Gasparik, 1990; Presnall and Walter, 1993], after [Ahrens, 1987]. Locations of dashed lines are inferred. Note that above 22 GPa perovskite + periclase melts to periclase + liquid, rather than perovskite + liquid. Wa represents Wadsleyite, Ring prepresents Ringwoodite.

et al. [1981] conducted shock recovery experiments on Fo in the range 78 to 92 GPa indicating that Pc (crystal) + $MgSiO_3$ (glass) is actually recovered from samples which were at high pressure for the short (10^{-7} s) time-scale of a shock wave experiment. The glass is inferred to be a reversion product of Pv from high pressure and temperature. Syono et al. noted that the Pc regions were several nanometers in diameter and the glass

was depleted in Si relative to Mg_2SiO_3. The diffusion constant inferred for a several nm region of MgO being produced in 10^{-7} s is $\sim 10^{-12.7}$ m^2/s. This value is compatible with diffusion data compiled by Brady [1995] for ^{30}Si in olivine, Ol, between 1430 and 1830 K.

1.2 Experimental details

In our experiments, a 25 mm-diameter lexan projectile bearing a 1.5 mm thick Cu, Ti, or Ta flyer plate is accelerated to 5 to 7 km/s. These impact 0.5 mm thick Cu, Ti, or Ta driver plates, inducing a planar shock wave in the driver plate. This shock then propagates into the natural olivine sample, inducing shock pressures ranging from 90 to 200 GPa [Ahrens, 1987]. Temperatures ranging from 4500 to 7000 K are produced by heating due to the irreversible work done on the sample by the shock wave.

In previous shock experiments using olivine crystals, Brown et al. [1988] inferred the pressure of the onset of melting of the assemblage Pc + Pv above ~140 GPa on the basis of a sharp decrease in longitudinal elastic wave velocity (Figure 1.3). Brown et al. also suggested that shock temperatures previously measured in Fo between 160 and 180 GPa [Lyzenga and Ahrens, 1980] represent the liquid regime of the Fo Hugoniot. As described later in Equation 1.1, Plank emissivity, ϵ_{ave}, is the factor which describes how a realistic Plank solid varies from a theoretically perfect black body. A material with ϵ_{ave} close to one emits with a high radiance for a given temperature, and a material with a lower ϵ_{ave} emits with a correspondingly lower radiance. Because Fo shocked below 160 GPa has a low ϵ_{ave}, temperatures in the pressure range where the Hugoniot curve crosses the solidus ($\sim$ 90 to 133 GPa) were not measurable (radiance less than 0.4×10^{12} $W/sr \cdot m^3$) [Lyzenga, 1982].

Here, we determine the onset of melting at lower pressures using natural Ol samples which have a higher emissivity, and a more sensitive optical pyrometer [Yang, 1996].

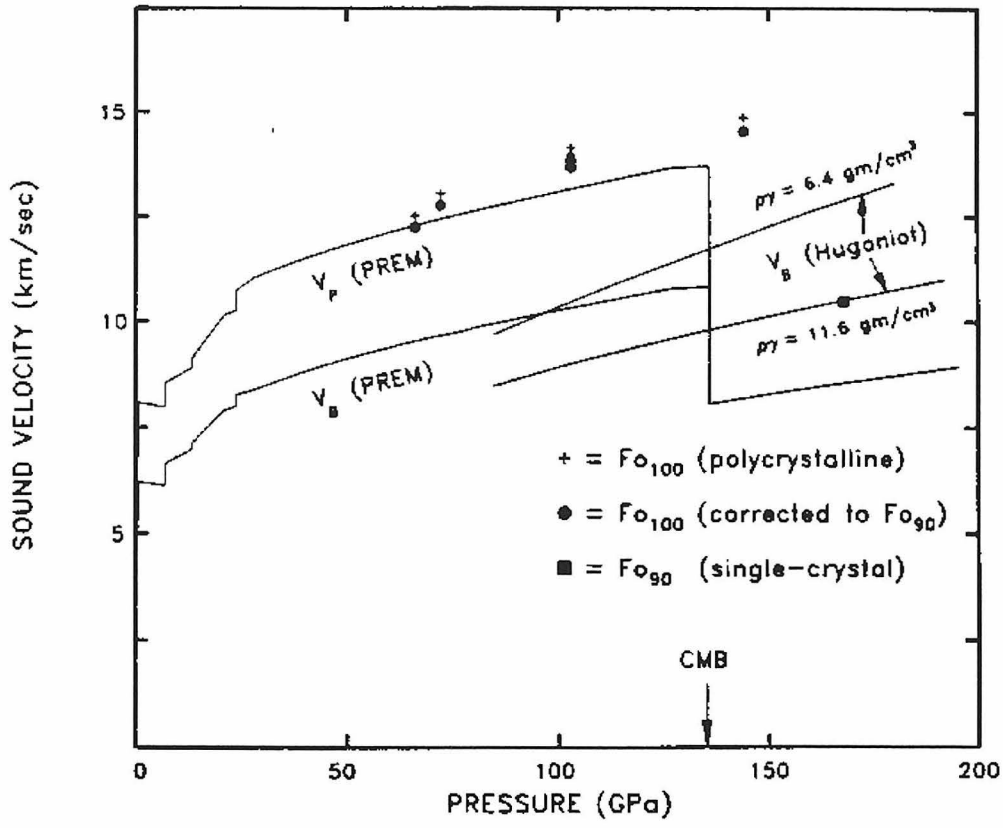

Figure 1.3: Sound speed-Compression curve for Ol(hpp), periclase + perovskite, after Brown et al. [1988]. The onset of melting is inferred to be above 140 GPa. The seismic model PREM [Dziewonski and Anderson, 1981] is shown for comparison.

We used samples of San Carlos and Burma peridot, for shock temperature experiments because they have a higher iron content and thus are green rather than transparent, so that they should have a higher emissivity at optical wavelengths. Electron microprobe (JEOL Super Probe) yielded analyses of San Carlos peridot as $(Mg_{0.91}, Fe_{0.09})_2SiO_4$ and Burma peridot as $(Mg_{0.89}, Fe_{0.11})_2SiO_4$. Hence the composition of all the samples is approximately $(Mg_{0.9}, Fe_{0.1})_2SiO_4$. Their ambient condition (STP) emissivities range from $\sim$ 0.7 to $\sim$ 1.0 for the optical range of 560 to 900 nm. Moreover, their solidi are within 110 K of the melting point of Fo at 1 bar, 2200 K [Pres-

nall and Walter, 1993], so the high pressure solidi of Fo(hpp) and Ol(hpp) are predicted to be similar [Jeanloz and Ahrens, 1977].

The optical pyrometer has 0.2 mm diameter photo-detectors, which give greater sensitivity and time resolution than our previous detectors but are harder to align. These have $0.005\frac{\mu W}{cm^2 nm}$ minimum resolvable intensity limit and 1 ns rise time as opposed to the $0.25\frac{\mu W}{cm^2 nm}$ and 15 ns rise times of the previous pyrometer [Boslough and Ahrens, 1989].

The 5 mm by 5 mm sample surface in contact with the driver plate is sputter-coated with an opaque layer of Ag to block light that may originate from the shock heated driver-sample interface [Lyzenga, 1982]. As the shock wave propagated through the 2 mm thick sample, the compressed region emitted thermal radiation, which then propagated through the balance of the absorbing unshocked sample. (Fig. 1.4).

The observed radiant intensity of a shocked solid depends upon the reflectivity of the shocked material/unshocked material interface, R_s, and the reflectivity of the unshocked material/vacuum interface at the free surface, R_f [Boslough, 1985].

$$I(\lambda) = \frac{\epsilon_{ave}\epsilon(\lambda)C_1 A_s(1-R_s)(1-A_u)(1-R_f)}{\lambda^5}[\ \exp[\frac{C_2}{\lambda T}] - 1]^{-1} \tag{1.1}$$

Here, $C_1 = 1.19088 \times 10^{-16}\ \mathrm{W \cdot m^2}$, and $C_2 = 1.4388 \times 10^{-2}\ \mathrm{m \cdot K}$. Temperature, T, and emissivity, ϵ_{ave}, are obtained from irradiance $I(\lambda)$ versus wavelength λ by fitting them to 1.1, using values for $\epsilon(\lambda)$, A_s, $1-R_s$, $1-A_u$, $1-R_f$ discussed below.

The unshocked sample transmission spectrum (Figure 1.5) is applied in three different ways in the analysis. (1) It is used to determine the photon fraction absorbed upon propagation from the emitting shock front through the unshocked sample, A_u. (2) The transmission spectrum is also used to estimate the wavelength dependence of emissivity, $\epsilon(\lambda)$, from the shocked material via Kirchhoff's law, absorbence equals emissivity.

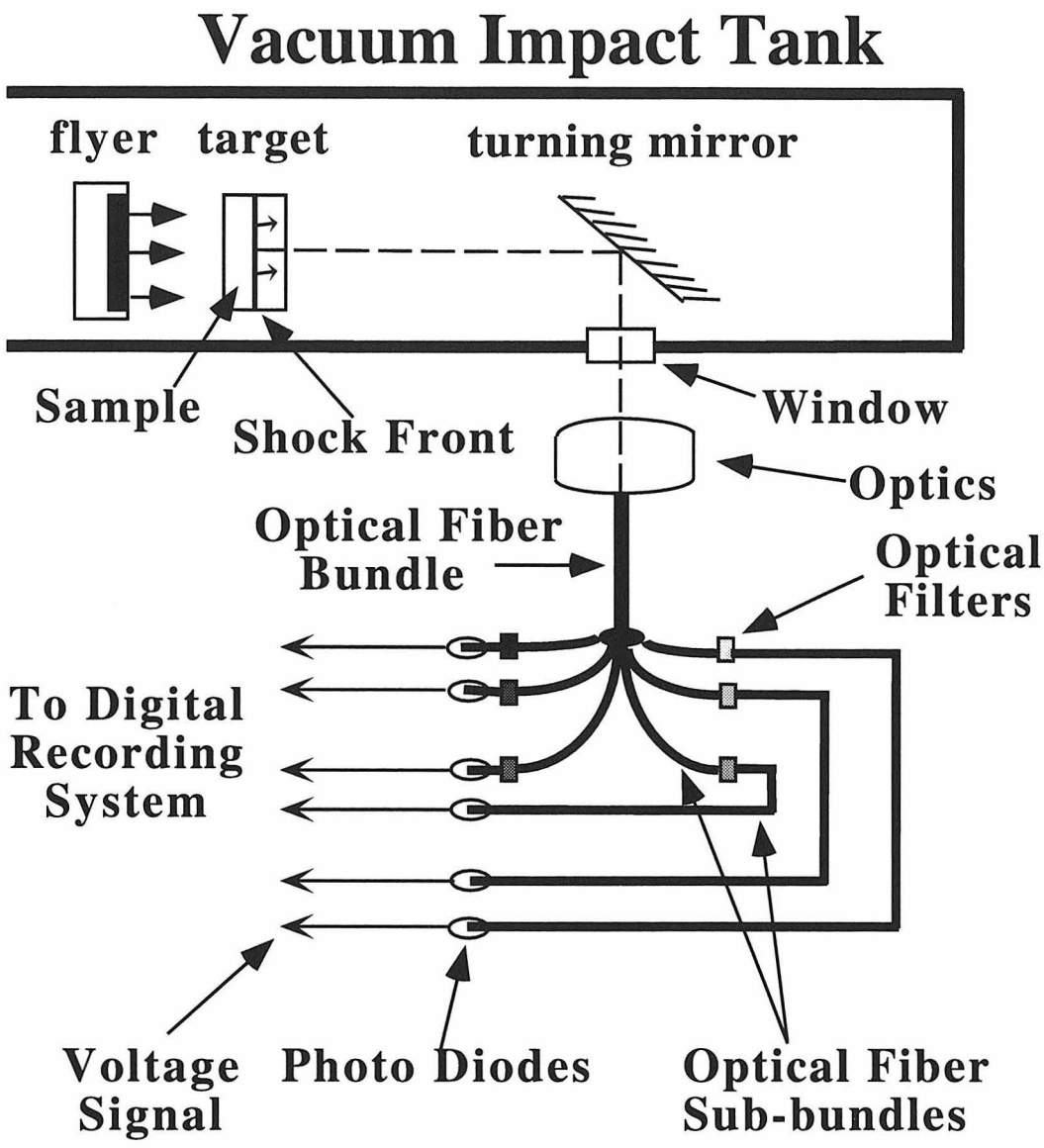

Figure 1.4: Schematic diagram of experimental setup [Ahrens, 1987]. Flyer is shown in flight before impacting sample. Shock front shown in sample as it would appear shortly after impact. Target and turning mirror are attached to impact tank, but the flyer is not. The impact tank is evacuated.

The value $\epsilon(\lambda)$ is normalized so that the maximum value is 1. Although ambient pressure values of transmittance were used to yield a wavelength-dependent emissivity for shocked olivine, this can only be considered an approximation. For instance, Fe_2SiO_4 demonstrates a marked reddening of absorption with increasing pressure at room tem-

perature, from 400 nm at 6 GPa to 700 nm at 14 GPa [Mao and Bell, 1972; Mao, 1973]. (3) Since data are scarce on the absorbence of shocked olivine, we must approximate $A_s = A_u$.

The reflectivities R_s and R_f are obtained from the index of refraction, via $R = (\frac{1-n}{1+n})^2$, where n is the ratio of the index of refraction for the two sides of the reflecting interface [Pedrotti and Pedrotti, 1987, page 479]. For the free surface reflection, we use the low pressure index of refraction of olivine $n_0 = 1.65$ and the index of refraction of the vacuum $n_v = 1$. For the reflection at the surface of the shock front, we use an estimate of the index of refraction at high pressure, $n_P = \frac{1.74+2.34}{2} = 2.04$, the average of the index of refraction of Pc and Pv, and n_0. Again, this is an approximation, employed because there are no experimental data for the index of refraction of the high pressure assemblage of $(Mg, Fe)_2SiO_4$.

As the shock front progressed through the sample, successively more shocked sample was radiating, and successively less unshocked sample was attenuating the radiation

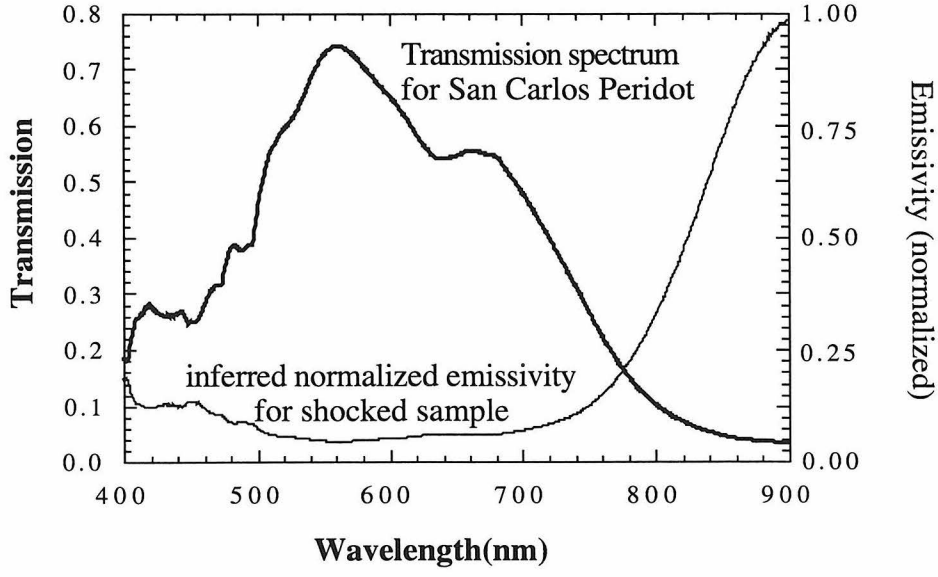

Figure 1.5: Transmission spectrum of natural olivine, San Carlos peridot which was used for shot # 279 and had a thickness of 1.741 ± 0.004 mm. The inferred normalized emissivity is shown with a lighter line, and the scale on the right.

from the shock front; thus, irradiance increased with time (Figure 1.6A). For each experiment, $\sim$ 300 ns duration signals were recorded for six wavelength bands from 450 to 900 nm. Since the sample emitted Planck radiation for only $\sim$ 300 ns, radiative losses did not significantly decrease the sample temperature [Svendsen et al., 1989]. Then the data were corrected for system response as described in Boslough [1985] and Section 3.7 of this thesis. Finally, the data were fitted to a Planck function to obtain emissivity and temperature (Figures 1.6 B through D). Shock temperatures were nearly constant (Figure 1.6C) during propagation through the sample whereas emissivity increased with time (Fig. 1.6B).

1.3 Experimental Results

We determined shock temperatures of peridot in eight experiments from 94 to 192 GPa (Table 1.1 and Fig. 1.7). Between 127 and 133 GPa, we measured a temperature change from 7041 $\pm$ 315K to 4292 $\pm$ 270K. The shock temperature data for peridot (reported here) and earlier data [Lyzenga and Ahrens, 1980] for the shock-induced melt of the high-pressure assemblage of Fo agree. The reported error-bars for the Ol(hpp) temperatures are $\pm$300 K but the scatter in the data is higher than that by a factor of 2. The emissivity, ϵ_{ave}, that is reported is the average of the last seven emissivities in the time series for the experiment, because the earlier emissivities were attenuated by the absorbing sample in the optical path. Also, the reported ϵ_{ave} does not contain wavelength dependence, since it is accounted for in the variable $\epsilon(\lambda)$, as detailed in Equation 1.1 and Figure 1.5. We infer that the difference in shock temperature observed between the 127 and 133 GPa experiments results from our observing the lower pressure metastable superheated (solid) hpp assemblage at 127 GPa, and the onset of melting regimes with increasing shock pressure at 133 GPa.

This behavior is analogous to that in SiO_2 and alkali halides. Lyzenga et al. [1983]

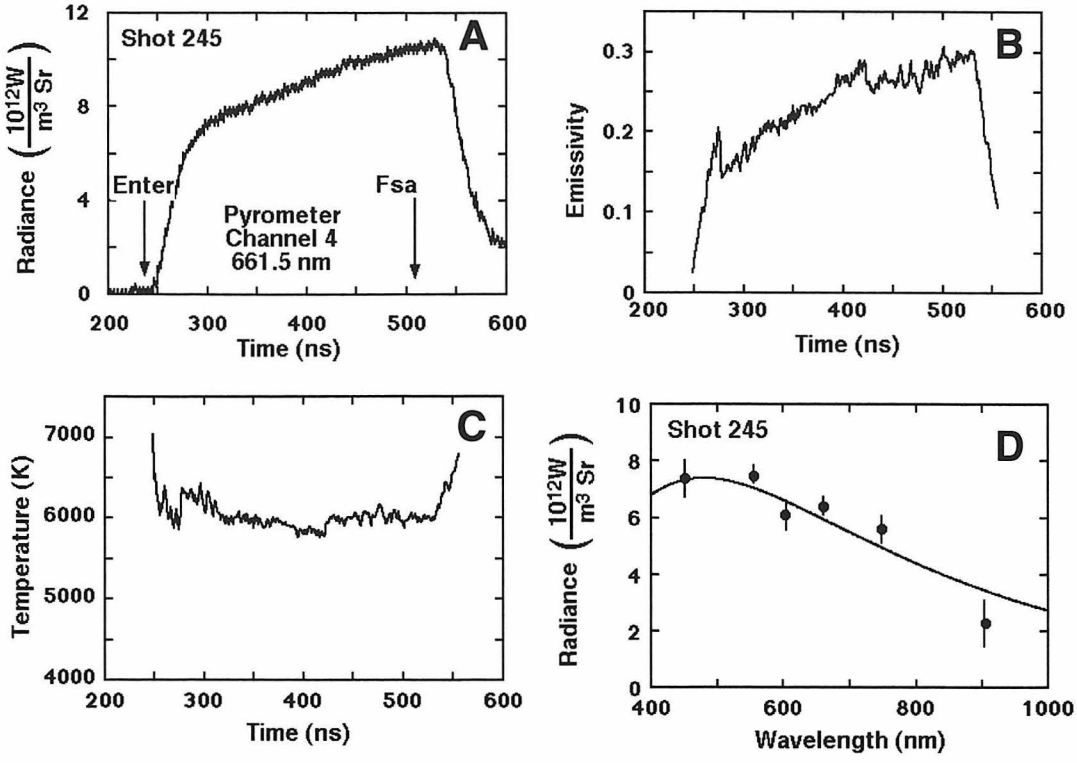

Figure 1.6: Experimental data for shocked olivine (A) Spectral irradiance versus time profile, centered at 650 nm, from Shot 245. The time marked "Enter" is the calculated arrival of the shock wave at the olivine, and "Fsa" is the calculated time of the shock wave arrival at the free surface of the olivine. (B) Spectral emissivity versus time for Shot 245. (C) Greybody temperature versus time for Shot 245. (D) Spectral fit of experimental radiant intensities at 522 ns for Shot 245. The solid line is the Planck curve for $T = 6092$ K and $\epsilon_{ave} = 0.226$.

reported similar appearing data sets for fused silica (FS) and crystalline quartz (Q) shocked into the stishovite regime that indicated melting of stishovite at 4500 and 4900 K at 70 and 110 GPa, respectively (Figure 1.8). Q and FS samples have different initial densities, and thus provide two points on the fusion curve of stishovite. The similarity between the Lyzenga et al. [1983] data and the data reported here is that the phase change from solid to liquid is represented by a discontinuity in the Hugoniot curve in the temperature versus pressure plane, and that the lowest point on the curve after the discontinuity is interpreted as a point on the fusion curve. Another analogous

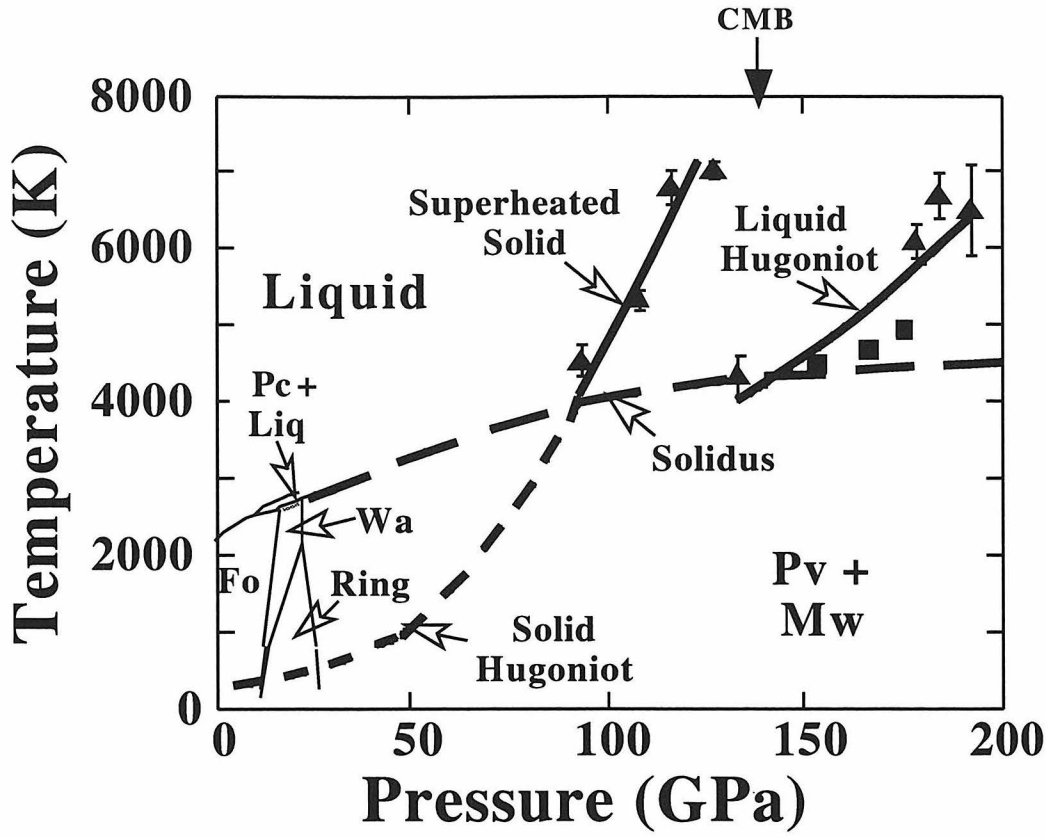

Figure 1.7: Pressure-temperature phase diagram for Mg_2SiO_4 and calculated Hugoniot temperature curve for Mg_2SiO_4. When the Hugoniot intersects the solidus, under equilibrium conditions, it would follow the solidus until complete melting occurs. However equilibrium is not achieved and Hugoniot states achieved overshoot the solidus due to kinetic effects. This results in states along a metastable extension of the solid Hugoniot, a phenomenon also observed in SiO_2 [Lyzenga et al., 1983] and in KBr and CsBr [Boness and Brown, 1993]. When melting occurs, experimental shock temperatures are inferred to lie along the solidus, substantially below the temperature of the super-heated solid. Data for San Carlos and Burma peridot (Table 1.1) are shown as solid triangles. Data for Fo [Lyzenga and Ahrens, 1980] are shown as solid squares, which have reported uncertainties of 200 K. The arrow marked CMB represents the pressure at the core-mantle boundary. Wa represents wadsleyite and Ring represents ringwoodite shown in detail in Figure 1.2.

Table 1.1: Temperatures of shocked olivine(hpp). ΔT and $\Delta\epsilon_{ave}$ are RMS uncertainties in temperature and emissivity for ~100 sample times during the last ~100 ns of radiative signal recorded for each shot.

shot #	Flyer/Driver material	Pressure GPa	Temperature K	ΔT K	Emissivity average	$\Delta\epsilon$ average
284	Cu/Cu	93.7	4545	321	0.22	0.15
244	Cu/Cu	107.8	5355	234	0.0132	0.0033
278	Cu/Cu	115.7	6800	201	0.51	0.17
289	Ti/Ti	127.1	7041	315	0.055	0.014
275	Cu/Cu	133.0	4292	270	0.038	0.048
245	Ta/Ta	178.4	6092	310	0.226	0.057
302	Ta/Ta	183.5	6700	213	0.0284	0.0091
303	Ta/Ta	192.0	6510	151	0.298	0.026

behavior is that recently, static diamond anvil data to 40 GPa are reported in melting data for SiO_2 (stishovite) [Shen and Lazor, 1995]. The extrapolation of the static SiO_2 data agrees closely with the melting temperatures of stishovite inferred by Lyzenga et al. [Ahrens, 1996], and the static Ol data of Presnall and Walter [1993] agrees closely with the melting temperatures of the high pressure assemblage of Ol inferred by this report (see Figure 1.7).

Boehler et al. [1996] finds good agreement between diamond cell and shock measurements for the melting of NaCl in the B2 structure at 3100 K and 55 GPa. NaCl in the B2 structure melts at 3100 K and 55 GPa [Ahrens et al., 1982; Boehler et al., 1996]. Additionally, Boness and Brown [1993] reported shock temperature and sound velocity data for KBr and CsBr, which demonstrate that these compounds are superheated and melt at higher pressures. Their behavior is qualitatively similar to that of

the natural olivines reported here. In the case of our $(Mg, Fe)_2SiO_4$ experiments, we favor the hypothesis that the drop in shock temperature at 130±3 GPa also results from melting. However, it is unclear whether the Hugoniot shocks up to the solidus or to the liquidus above 130 GPa when pressures are large enough to overcome the metastable superheated state.

One can also examine whether the temperature difference observed between the 127 and 133 GPa experiments could possibly result from a solid-solid phase change.

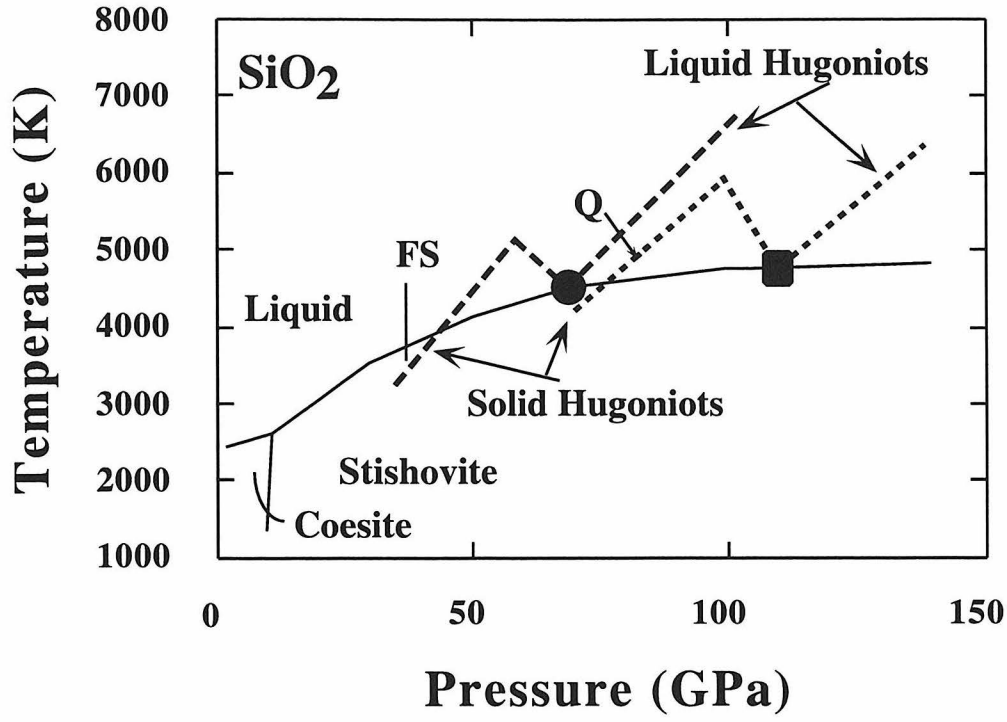

Figure 1.8: Shock temperatures of SiO_2 starting from fused quartz shocked into the stishovite regime and the upper bound to the solidus of stishovite (after Ahrens [1996]). The dashed lines represent Hugoniot data of Lyzenga et al. [1983]. The low pressure phase boundaries are from Shen and Lazor [1995]. Ahrens [1996] interpretation of the Lyzenga et al. data is that the stishovite/liquid phase boundary passes through the lowest points on Hugoniot data after the drop in temperature. FS is fused silica, and Q is quartz. The solid dot is the point on the solid/liquid phase boundary inferred from the FS data, and the solid square is the point on the solid/liquid phase boundary inferred from the Q data.

A discontinuity in sound velocity versus pressure, which is attributed to melting, is observed at $\sim$ 140 GPa [Brown et al., 1988](see Figure 1.3). Additionally, an increase in density for a hypothetical solid-solid phase change (rather than melting) cannot be greater than $\sim$1-2%. If the 2700 $\pm$ 585 °C decrease in shock temperature at $\sim$ 130 GPa were associated with a solid-solid reaction, an estimate of the enthalpy change, ΔH, would be given by $\Delta H = C_v \Delta T =$ 480 kJ/mole for a specific heat of $C_v = 3R_u$, where R_u is the universal gas constant. This value is considerably greater than the enthalpies associated with melting under equilibrium conditions ($\sim$ 115 kJ/mole) or the 97 kJ/mole required for the STP reaction Mg_2SiO_4 (Ringwoodite) $\rightarrow MgSiO_3$(Pv)+MgO(Pc). The lack of a sharp density increase along the Hugoniot in the regime where the density agrees with that expected for Pc + Pv taken with the associated drop in sound velocity at $\sim$ 140 GPa supports the inference that Pc + Pv is melting rather than undergoing a solid-solid phase transition.

Chen et al. [1996] suggest that the formation of wadsleyite (Wd) and ringwoodite (Ri) requires special conditions, such as elevated temperatures of the target before shock compression, which would imply that the conditions achieved in our dynamic impact experiments are not sufficient to produce Pc + Pv. This might be construed as a possible alternative explanation of why we do not observe a phase change between 90 and 130 GPa. We contend that the inhibition of the transformation is kinetic rather than thermodynamic, because the shock-induced minerals Wd and Ri are found in meteorites, such as Tenham and Catherwood [Madon and Poirier, 1983]. Meteorites experience shock-loading conditions similar to those created in laboratories, except that the high pressure is held for much longer times than laboratory experimental samples, 10^{-5} s as opposed to 10^{-7} s, due to their much larger size, 10's of cm, as opposed to mm's. Since the reaction occurs when allowed 10^{-5} s, but does not occur when allowed 10^{-7} s, we conclude that the inhibition of the phase change is kinetic in the laboratory experiments.

Because a material will not melt if its temperature does not exceed the solidus at the relevant pressure, the most conservative interpretation of our data is that the observed shock temperature at 4300 ± 270 K represents an upper bound to the solidus of 130 ± 3 GPa. Whether or not a more realistic interpretation is that 4300 K represents the liquidus requires further study. Additionally, there is the possibility that the onset of melting could be over-driven by kinetic effects [Boness and Brown, 1993], so again our estimated solidus is an upper bound. Our estimate to the upper bound of the solidus is consistent with a reasonable extrapolation up to 130 GPa of a solidus attained for $(Mg_{0.9}, Fe_{0.1})_2SiO_4$ at 7 – 16.5 GPa pressure reported by Presnall and Walter [1993] (see Figure 1.2).

1.4 Speculative MgO - SiO_2 phase diagram

The MgO - SiO_2 phase diagram is of interest because Ol, Pv and Mw are dominant minerals in the Earth. Ignoring Fe content, the bulk composition of the lower mantle lies between MgO and $MgSiO_3$ [Allègre et al., 1995; Weidner, 1986; Stixrude et al., 1992; Jeanloz and Morris, 1986]. Thus, in order to study the behavior of the lower mantle, previous authors have concentrated on studying the high pressure behavior of MgO and $MgSiO_3$ [Knittle and Jeanloz, 1989; Zerr and Boehler, 1993; Sweeney and Heinz, 1997]. We have concentrated on studying the high pressure behavior of $(Mg, Fe)_2SiO_4$.

At 1 bar and 298 K, the stable phases in the MgO – SiO_2 system are Pc, Fo, Pv, and Q, having compositions (in % SiO_2.) of 0.0, 0.33, 0.5, and 1.0 respectively. Figure 1.9 A) shows the temperature versus composition phase diagram for the MgO – SiO_2 system at 1 bar (O GPa). Materials with a composition between 0.0 and ~0.3 exsist as phases Pc + Fo at 298 K. At higher temperature, Pc + Fo → Pc + Liq. At even higher temperature the material melts to a single liquid of the initial composition. For materials of a composition between ~0.3 and 0.33, Pc + Liq. → Fo + Liq. For materials

of a composition between 0.33 and 0.5, the initial material is Fo + En (enstatite). At higher temperatures Fo + En $\rightarrow$ Fo + Liq. For materials of a composition between 0.5 and $\sim$0.55, the initial material is En + Tr (Tridymite). At higher temperatures, En + Tr $\rightarrow$ En + Cr (cristobalite), a solid–solid phase change. At even higher temperatures, En + Cr $\rightarrow$ En + Liq. For materials with an initial composition between $\sim$0.55 and $\sim$0.65, En + Tr $\rightarrow$ En + Cr, then En + Cr $\rightarrow$ Cr + Liq. For materials with initial composition between $\sim$0.65 and $\sim$0.97, En + Tr $\rightarrow$ En + Cr, then En + Cr $\rightarrow$ En + Cr $\rightarrow$ Cr + Liq., then Cr + Liq. $\rightarrow$ Liq. + Liquid2.

In constructing phase diagrams for higher pressures, one must use the available experimental data. Solidus temperatures have been measured for MgO up to 35 GPa [Zerr and Boehler, 1994]. Solidus temperatures have been measured for $MgSiO_3$ up to 60 and 96 GPa [Zerr and Boehler, 1993; Knittle and Jeanloz, 1989; Heinz et al., 1994]. In our constructed phase diagrams, the Zerr and Boehler [1993] temperatures are used, but interpretations based on the data of Knittle and Jeanloz [1989] are explored afterwards. The high pressure data for $(Mg, Fe)_2SiO_4$ and for SiO_2 are obtained for pressures of 130 GPa and for 70 and 90 GPa, respectively. As discussed above in relation to Figure 1.7, the most conservative interpretation of this kind of data is that 4300 K is an upper bound to the solidus, but it is unclear if a more realistic interpretation is that 3400 K is a point on the liquidus. Therefore, we have constructed two sets of high pressure phase diagrams. Figure 1.9 assumes that shock temperature experiments probe liquidus temperatures, and Figure 1.10 assumes shock temperature experiments probe solidus temperatures.

We constructed phase diagrams at 50 GPa, Figures 1.9 B) and 1.10 B), by employing Zerr and Boehler's extrapolation of their MgO data from 35 GPa to 50 GPa, using the $MgSiO_3$ data at 50 GPa, interpolating between our $(Mg, Fe)_2SiO_4$ data at 130 GPa and Presnall's data at 15 GPa, and interpolating between Lyzenga's SiO_2 data at 70 GPa, and Shen and Lazor's data at 45 GPa.

We constructed phase diagrams at 130 GPa, Figures 1.9 C) and 1.10 C), by employing Zerr and Boehler's extrapolation of their MgO data from 35 GPa to 130 GPa, extrapolating the $MgSiO_3$ from 60 GPa to 130 GPa, using the $(Mg,Fe)_2SiO_4$ data at 130 GPa, and extrapolating the SiO_2 data from 110 GPa to 130 GPa.

In order to determine the details of Figures 1.9 and 1.10, it is necessary to consider the issue of whether the MgO - $MgSiO_3$ system melts as solid-solution type system or a eutectic-type system. If it is a eutectic system, it is necessary to consider whether or not the system has a binary compond. At low pressures, the MgO - $MgSiO_3$ system acts as a eutectic with a binary compound, because Mg_2SiO_4 (olivine) is a stable phase (see Figure 1.9, 0 GPa). However at pressures greater than 22.5 GPa the stable assemblage for Mg_2SiO_4 is Pc + Pv (see figure 1.2). The solidus of Mw + Pv ($(Mg,Fe)O+(Mg,Fe)SiO_3$) at 130 GPa inferred from this study is lower than the extrapolated solidi for both Pv and for Pc as measured statically [Knittle and Jeanloz, 1989; Zerr and Boehler, 1993, 1994]. Thus, we infer that at 130 GPa the MgO - $MgSiO_3$ system is a eutectic system without a binary compound. A similar argument can be given to show that the MgO - $MgSiO_3$ system at 50 GPa is also a eutectic system without a binary compound.

The eutectic compositions at 50 GPa are shown as being between the compositions for $MgSiO_3$ and Mg_2SiO_4, because at low pressure (16 - 21 GPa) Mg_2SiO_4 is observed to undergo partial melting to Pc + liq, as shown in Figure 1.2. The assumption that the eutectic composition does not move much closer to MgO at higher pressures is of course simplistic and may be incorrect. Experimental data are needed at high pressures in order to solve this ambiguity. The most conservative assumption is that this does not change at higher pressures, so we have drawn it as such. However the actual details of the phase diagram are presently unknown.

Figure 1.11 shows a comparison of the liquidi as a function of composition with pressure contours. This highly speculative diagram serves to illustrate how little is actually known about the MgO - SiO_2 system at high pressures. The dots represent the

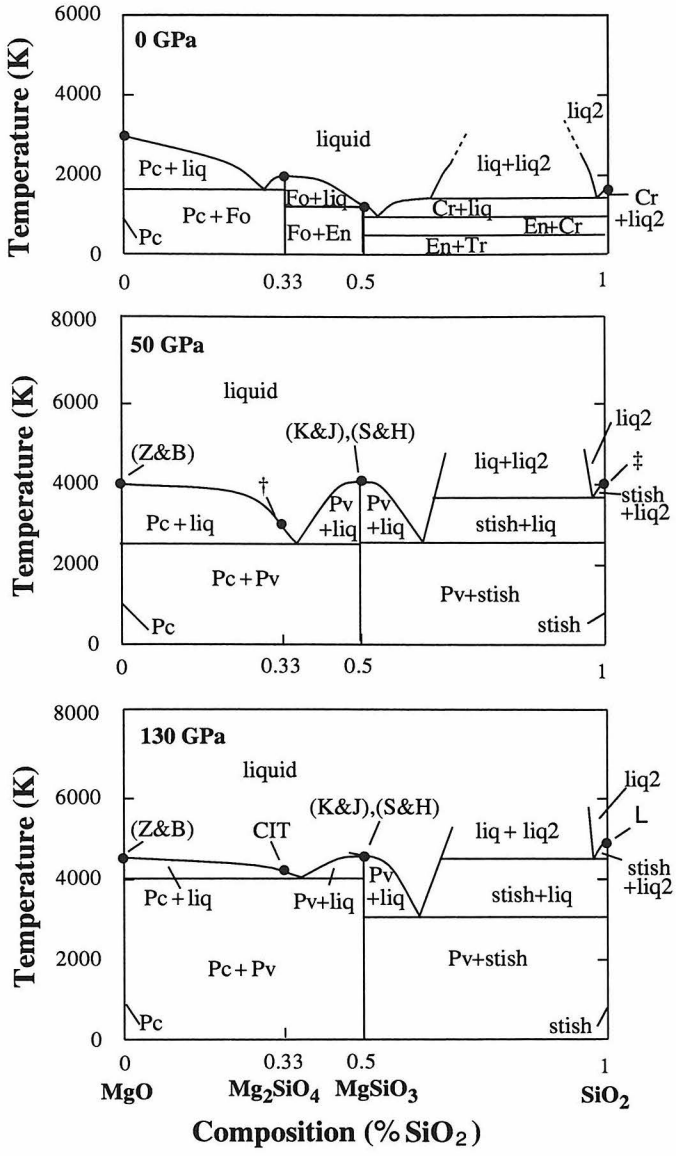

Figure 1.9: The phase diagram for the MgO – SiO_2 system, assuming that our experiments measured the liquidus of $(Mg, Fe)_2SiO_4$. A speculative interpretation of melting data for MgO [Zerr and Boehler, 1994], $(Mg, Fe)_2SiO_4$[this thesis], $MgSiO_3$ [Knittle and Jeanloz, 1989; Zerr and Boehler, 1993], and SiO_2 [Lyzenga et al., 1983; Shen and Lazor, 1995; Ahrens, 1996] are shown as solid dots. Phase diagrams for 0 GPa [Bowen and Anderson, 1914; Greig, 1927], 50 and 130 GPa are presented. Abbreviations are as follows: CIT - this thesis, † - interpolation between Presnall and Walter [1993] and CIT, K&J - Knittle and Jeanloz [1989], S&H - Sweeney and Heinz [1997], Z&B - Zerr and Boehler [1994], L - Lyzenga et al. [1983], ‡ - interpolation between L and Shen and Lazor [1995], Pc - periclase, Pv - perovskite, stish - stishovite, Fo - forsterite, En - enstatite, Tr - tridymite, Cr - crystobalite.

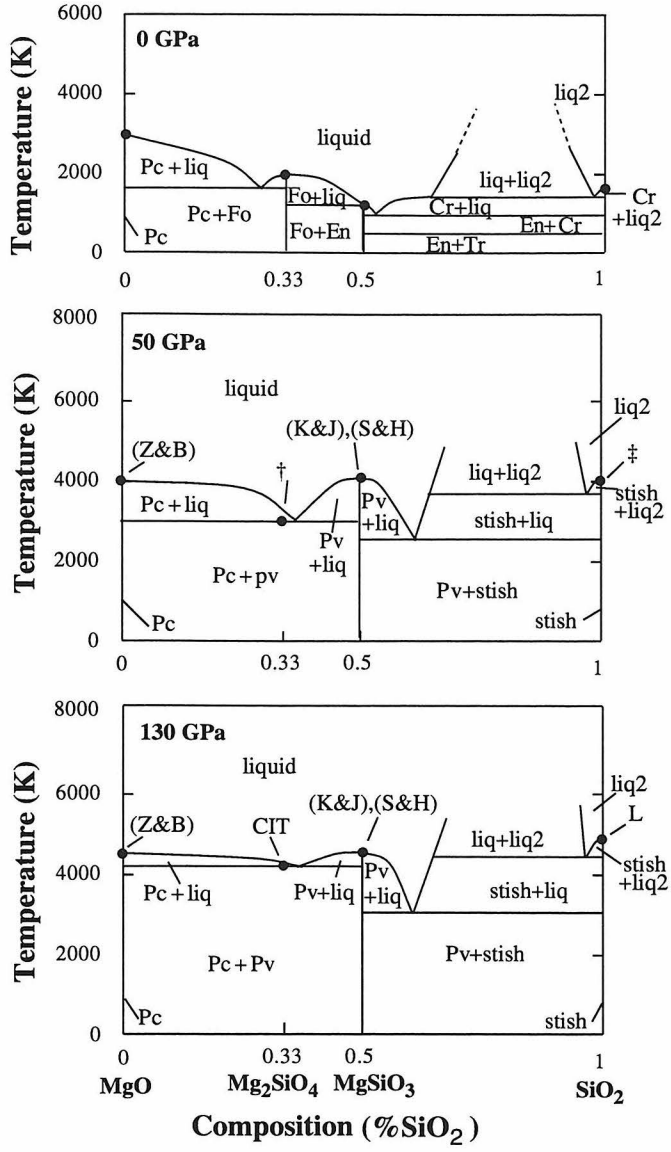

Figure 1.10: The phase diagram for the MgO – SiO_2 system, assuming that our experiments measured the solidus of $(Mg, Fe)_2SiO_4$. A speculative interpretation of melting data for MgO [Zerr and Boehler, 1994], $(Mg, Fe)_2SiO_4$[this thesis], $MgSiO_3$ [Knittle and Jeanloz, 1989; Zerr and Boehler, 1993], and SiO_2 [Lyzenga et al., 1983; Shen and Lazor, 1995; Ahrens, 1996] are shown as solid dots. Phase diagrams for 0 GPa [Bowen and Anderson, 1914; Greig, 1927], 50 and 130 GPa are presented. Abbreviations are as follows: CIT - this thesis, † - interpolation between Presnall and Walter [1993] and CIT, K&J - Knittle and Jeanloz [1989], S&H - Sweeney and Heinz [1997], Z&B - Zerr and Boehler [1994], L - Lyzenga et al. [1983], ‡ - interpolation between L and Shen and Lazor [1995], Pc - periclase, Pv - perovskite, stish - stishovite, Fo - forsterite, En - enstatite, Tr - tridymite, Cr - crystobalite.

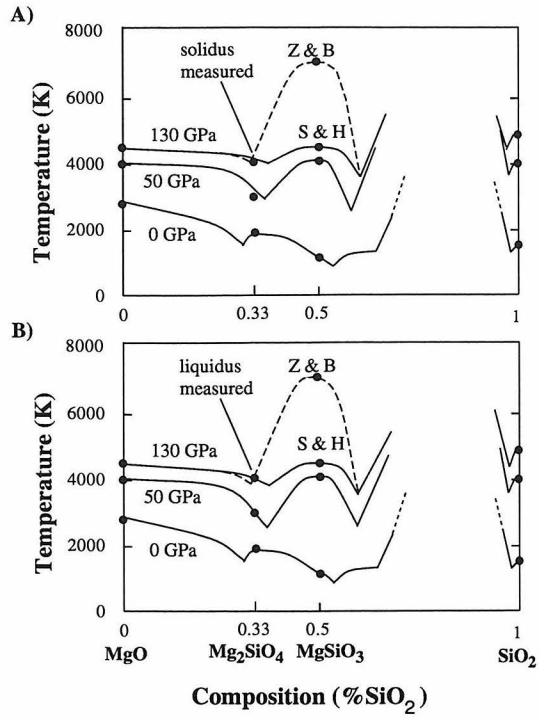

Figure 1.11: Comparison of high-pressure liquidus temperatures from Figures 1.9 and 1.10. A) liquidus temperatures assuming our $(Mg, Fe)_2SiO_4$ experiments measured solidus temperatures. B) liquidus temperatures assuming our $(Mg, Fe)_2SiO_4$ experiments measured liquidus temperatures. The 130 GPa curve shows both a high estimate for the melting temperature of Pv based on Zerr and Boehler [1993] (Z&B), and a low estimate based on Knittle and Jeanloz [1989] and Sweeney and Heinz [1997] (S&H)

only data available on the system. Note that at 130 GPa, the range of estimates of the melting temperature of $MgSiO_3$, are disparate and it is critical that more work be done in this area so that this issue may be resolved. If the higher estimate is assumed for the melting temperature of $MgSiO_3$, then the slope of the curves approaching eutectic composition are much steeper, and the actual eutectic composition must be very close to Mg_2SiO_4 in order to keep the eutectic temperature from being unrealistically low, although the composition of the eutectic may very well be less than 0.33 percent SiO_2. If the lower estimate is assumed for the melting temperature of $MgSiO_3$, then the slope

of the curves approaching eutectic composition are shallower and the composition of the eutectic is less well constrained. However both estimates are consistent with the suggestion that in the $MgO-MgSiO_3$ system, the high-pressure lower mantle assemblage can undergo eutectic melting and the eutectic lies between the composition Mg_2SiO_4 and $MgSiO_3$.

1.5 Conclusion

The results of Stixrude et al. [1992] imply that the lower mantle of the Earth can be modeled as an intimate mixture of Pc + Pv. We have measured an upper bound to the solidus of Pc + Pv at ~4300 K at ~130 GPa. Thus we infer the Earth has an upper bound to its solidus of 4300 K at the pressure of the core-mantle boundary (CMB).

Furthermore, the upper bound to the solidus of Pc + Pv at 130 GPa is lower than the extrapolated values of the solidus of either Pc or Pv, so the lower mantle assemblage is a eutectic system, and its eutectic composition is near Mg_2SiO_4.

Chapter 2

Shock temperature of stainless steel and a constraint on the high pressure - high temperature thermal diffusivity of Al_2O_3

2.1 Introduction

Experimental data on the temperatures and pressures of phase transitions in iron and iron alloys are important in understanding thermodynamic processes in the deep earth. This is discussed in detail in Chaper 4 of this thesis. In this chapter, we report a new target configuration which can be used to constrain thermal diffusivity of Al_2O_3 at high pressure, which is used to constrain the temperatures of shock induced phase transitions. We then discuss an approximate analytic heat flow model for this new target configuration, and present transient temperature versus time results for this configuration. We demonstrate how to obtain ratios of thermal diffusivity for stainless steel-Al_2O_3

and then use the new experimentally constrained diffusivity ratios to calculate Hugoniot temperatures for stainless steel from interface temperatures and other parameters. Then we report those values in a phase diagram for stainless steel and compare the Hugoniot temperatures of stainless steel to those of iron (from Chapter 3 of this thesis). Finally, we discuss the systematics of this comparison to support the empirical quality of Al_2O_3 as transparent anvil material for metal shock temperature experiments.

2.2 Previous work on the Hugoniot of stainless steel and iron

Several previous studies on the shock temperatures of metals have been reported in which thermal radiation emitted from an interface between the metal and a transparent anvil (e.g. Al_2O_3) is measured to obtain Planck interface temperatures, T_i, and emissivities, ϵ_{ave} [Urtiew and Grover, 1974; Williams et al., 1987; Bass et al., 1987; Tan and Ahrens, 1990; Ahrens et al., 1990b,a]. These interface temperatures are used to infer the Hugoniot temperature of the metal, $T_{h,m}$, as a function of shock pressure, $P_{h,m}$. In these experiments, $P_{h,m}$ is calculated from previously measured equations of state [Ahrens and Johnson, 1995] and measured impact speed, via the impedance match method [Ahrens, 1987].

The first attempted measurements of shock temperature data for metals were overwhelmed by Planck radiation emitted from irregularities at the metal-transparent anvil interface [Urtiew and Grover, 1974]. The problem was overcome by using windows in which a thin 10 μm layer of sample material was sputtered onto the anvil, yielding the first shock temperature data for iron at 200 to 300 GPa [Bass et al., 1987]. Williams et al. [1987] compared these first shock temperatures with his static measurements of the solidus of iron up to 100 GPa to present the first high pressure phase diagram for iron.

Tan and Ahrens [1990] used a data analysis method which studies the released state of the shocked metal (Figure 2.1). The phase boundary acts as a temperature buffer, so that when studying a $T_{h,m}$-$P_{h,a}$ data set for a particular material more points along the phase boundary can be determined than if only Hugoniot states were considered. Ahrens et al. [1990a] reanalysed the shock temperatures for iron from Bass et al. [1987] to take into account the analysis method of Tan and Ahrens [1990]. Ahrens et al. [1990b] critically reviewed the experimental results to date and chose four experiments as having the best data quality and also presented four new experiments on shock temperatures for stainless steel.

Previous calculations of McQueen et al. [1970] predict a lower shock temperature

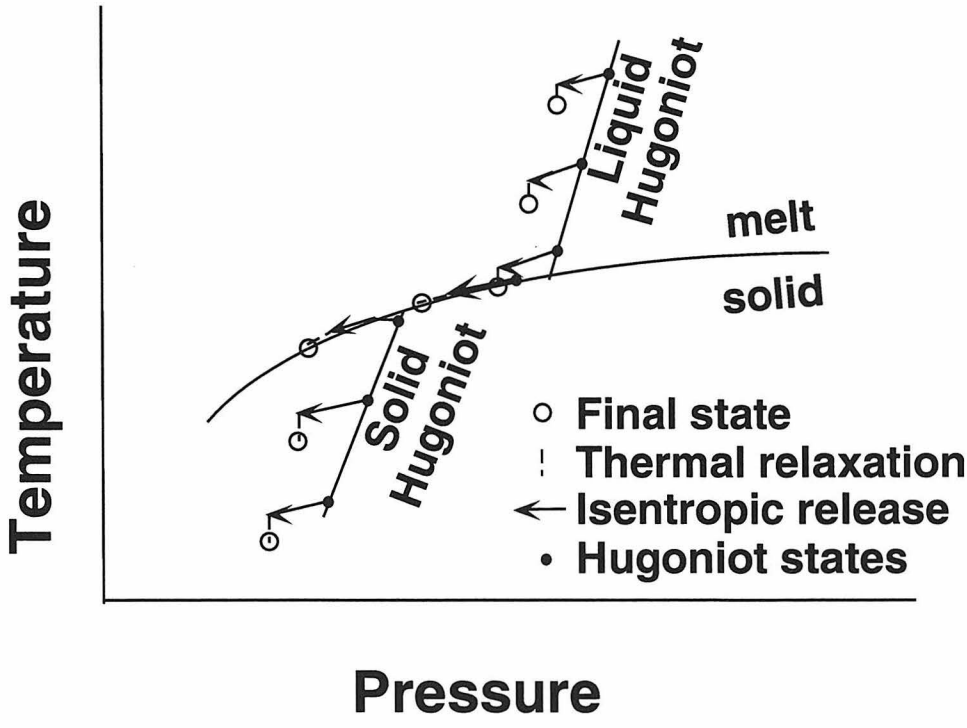

Figure 2.1: Hugoniot states and pressure release paths followed during a shock temperature experiment. Tan and Ahrens [1990] calculated temperature-pressure paths to obtain further information about temperatures along a phase boundary. At the metal anvil interface, Hugoniot temperatures, ($T_{h,m}$,$P_{h,m}$), represented by the solid circles release to interface temperatures, (T_i,$P_{h,a}$), represented by open circles.

for 304 stainless steel (SS) than for iron, at a given pressure. This study focuses on a measurement of the shock temperatures of stainless steel and of the high pressure thermal diffusivity ratio of the stainless steel and the anvil at the metal-anvil interface. We also address the issue of verifying the predicted systematic difference between the measured shock temperatures of SS and iron at the same pressure. Several authors have suggested that the detected thermal radiation in these experiments is not actually emitted from the metal- transparent anvil interface, but rather is emitted from the shocked anvil material [Nellis and Yoo, 1990; Kondo, 1994]. If our measurements are consistent with the predictions of McQueen et al. [1970], then it can be inferred that the thermal radiation is emitted from the metal–anvil interface rather than from within the shocked anvil material. Also, if two different anvil materials are used, such as LiF and Al_2O_3, the consistency of the observed interface temperatures can be used to further demonstrate whether a significant contribution from the thermal radiation originates within the anvil.

In previous shock temperature studies [Bass et al., 1987; Ahrens et al., 1990b], the target configuration used metal drivers and $\geq$ 10 μm thick films, predicting no measurable decrease in the interface temperature with time [Grover and Urtiew, 1974]. The previous authors related T_i to $T_{h,m}$ as detailed in Chapter 3, Section 3.2. There are also uncertainties in the values of parameters that are used in the calculation of $T_{h,m}$ from T_i, such as the high pressure thermal diffusivity ratio of the anvil and the iron sample.

2.3 Methods

Previous studies used the "Traditional" target configuration shown in Figure 2.2 A. For this configuration the interface temperature is not expected to decrease with time and it is dependent on the $T_{h,m}$ (see Appendix A, Equations A.8 and A.9). We employ

a new "sandwich" configuration that has a thinner film (1 μm thick) and the same material for the anvil and the driver. This allows heat to diffuse out of the hot metal into the relatively cold anvil material at a rate fast enough that the temperature is expected to decrease at the interface. The magnitude of the temperature decrease with time is dependent on the thermal diffusivities (at the temperature and pressure of the experiment), κ_m and κ_a, of the metal and the anvil, respectively (Section 2.5). The diffusivities, κ_m and κ_a, are dependent upon thermal conductivities, k_m and k_a, as expressed later in Equation 2.6. The thermal conductivity of the metal, k_m, is well constrained by the Wiedemann-Franz law,

$$k_m = L\sigma T_h \tag{2.1}$$

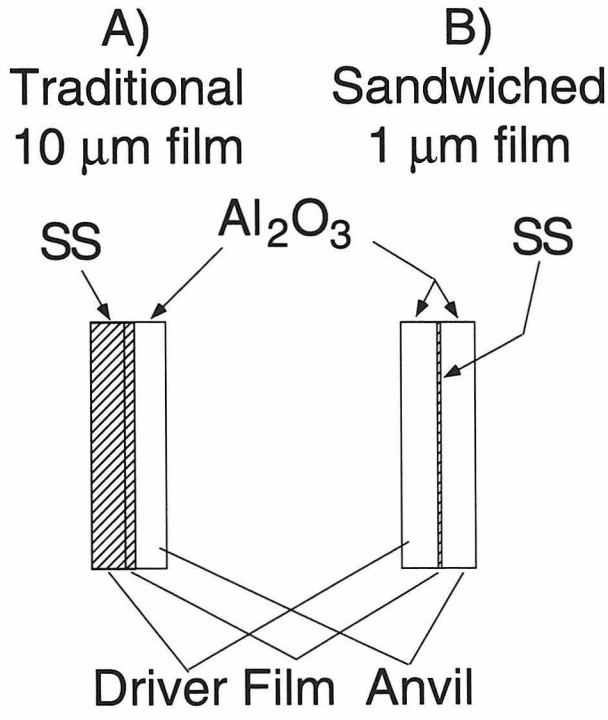

Figure 2.2: Target configurations A) Previous target with a stainless steel (SS) driver and a thick (10 μm) film. B) "Sandwich" configuration with a thin (1 μm) film, and anvil and driver of the same material (Al_2O_3).

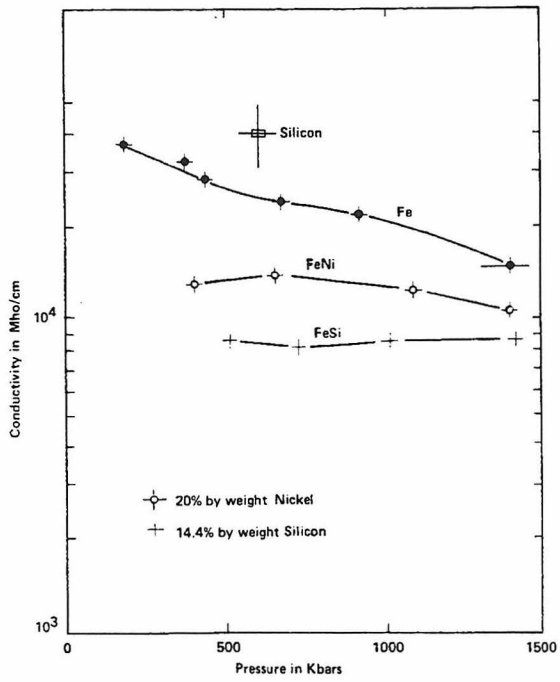

Figure 2.3: Electrical conductivity data of geophysical interest, after Matassov [1977]. Electrical conductivities were measured in situ under shock loading, as a function of Hugoniot pressure, $P_{h,m}$ (and the corresponding Hugoniot temperature, $T_{h,m}$). Solid circles represent Fe, open circles represent $Fe_{0.81}Ni_{0.19}$, pluses represent $Fe_{0.75}Si_{0.25}$.

where σ is electrical conductivity and $L = 2.45 \times 10^{-8}\ W\Omega/K^2$. There are no experimental measurements of σ for stainless steel, but Matassov [1977] measured σ for Fe and other materials of geophysical interest, FeNi, FeSi, and Si (Figure 2.3). To calculate k_m we used Matassov's conductivities for iron. In order to improve this calculation, electrical conductivity experiments need to be conducted on stainless steel. We conducted two experiments (Shot numbers 271 and 278) employing the "Sandwiched" configuration shown in Figure 2.2 B. Here the driver material is the same as the anvil material and the metal is 1 μm thick. In this geometry, after the shock wave traverses the metal, the thin metal is sandwiched between two cooler pieces of the material which are the anvil and driver. The resulting heat flow should be symmetric about the center plane

of the metal film as modeled analytically below. Moreover, heat conduction occurs such that, on the time scale of the present experiments ($\sim$ 250 ns), the interface temperature can be observed to decrease.

Thus, we are effectively measuring the thermal diffusivity ratio of the anvil/metal interface at high pressure. We assume that specific heats are well known for both media. When a decrease in radiation with time is observed, it could be argued that some or all of the decrease could be due to a change in the anvil material opacity [Boslough and Ahrens, 1989]. On the other hand, for film thicknesses of 10 μm, no measurable temperature decrease is expected due to thermal diffusion. Thus if we employ 10 μm films and observe no measurable temperature decrease, then we can conclude that the anvil material remains transparent.

Calculations discussed in Section 2.5 show that a resolvable temperature decrease of 500 K should be detectable in a $\sim$250 ns time interval. This is approximately the time required for the shock propagation through the anvil.

The SS samples were made from the same sputtering target used to make the samples of Ahrens et al. [1990b] so their chemical composition is assumed to be the same (Table 2.1). The radiation from the target was measured using a 6 channel pyrometer (Figure 2.4). The radiation calibration was performed with a tungsten ribbon filament lamp in a procedure similar to that of Boslough and Ahrens [1989], and described in detail in Section 3.7 of this thesis. The shock experiments were performed on the Caltech two stage light gas gun. Projectile speeds were in the range of 5.4 km/s to 6.8 km/s, resulting in shock pressures between 231 and 321 GPa. Tantalum flyer plates were employed and the shock pressures were calculated using the same parameters for equation of state of Ta, SS, Al_2O_3 and LiF as in our previous work [Ahrens et al., 1990b], and references therein.

2.4 Experimental Results

The observed radiation intensities, corrected with the calibration data, were fit to the Planck function using an iterative least squares method to obtain the T_i and emissivity, ϵ_{ave}. The emissivity was assumed to be wavelength independent for this calculation. Then the temperature was corrected from T_i to the shock Hugoniot temperature, $T_{h,m}$ (Table 2.2 and Figure 2.5) as explained in detail in Chapter 3 and by Ahrens et al. [1990b]. In Figure 2.5 the solid symbols represent Hugoniot temperatures at Hugoniot pressures. The open symbols represent the type of shock temperature data analysis reported by Tan and Ahrens [1990] and diagrammed in Figure 2.1. The arrow represents the pressure at which Hixon et al. [1994] observed a decrease in sound speed that appears

Table 2.1: Chemical composition of stainless steel samples in weight percent, after Ahrens et al. [1990b]

Element	316 Stainless Steel Film Present Samples	316 Stainless Steel *
Fe	69.3	68.0
Cr	19.4	19.0
Ni	9.1	10.0
Mn	—	2.0
Si	0.7	1.0
C	—	0.08
Total	98.5	100.08

* McQueen et al. [1970]

Table 2.2: Hugoniot temperatures, $T_{h,m}$, and best fit emissivities, ϵ_{ave} of stainless steel (SS). Shot #'s, anvil materials used, and Hugoniot pressures of the anvil and stainless steel, $P_{h,a}$ and $P_{h,m}$, are given for reference.

Shot	$P_{h,m}$	Anvil	$P_{h,a}$	$T_{h,a}$	T_i	ϵ_{ave}	$\Delta\epsilon_{ave}$	$T_{h,m}$	$\Delta T_{h,m}$
	SS		anvil	anvil	SS	SS	SS	SS	SS
#	(GPa)	mat.	(GPa)	(K)	(K)			(K)	(K)
277	222	LiF	125	2850	3931	0.64	0.04	5092	410
247	236	Al_2O_3	140	1100	4410	0.24	0.01	5800	370
228	257	Al_2O_3	182	1670	4538	0.33	0.02	5988	440
227	263	LiF	146	3530	4243	0.44	0.03	5940	400
271	274	Al_2O_3	208	2110	4739	0.32	0.02	6160	550
270	295	Al_2O_3	216	2250	5342	0.22	0.01	6247	620
246	311	LiF	223	6440	5768	0.16	0.01	7420	330
278	321	Al_2O_3	241	2730	6080	0.20	0.01	8440	430

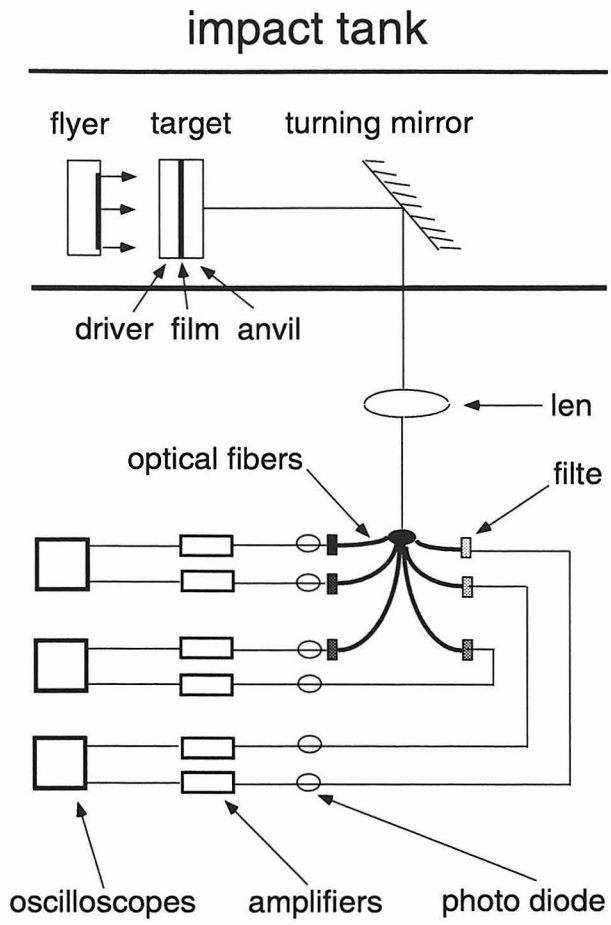

Figure 2.4: Six channel optical pyrometer. Lens projects target image onto optical fiber bundle. Bundle is split into 6 sub-bundles which lead to 650 nm wide optical filters, 6 photodiodes and 6 linear amplifiers. Resultant signals are recorded on oscilloscopes.

to correspond to melting. Shots 271 and 278 indicated by "S" in Figure 2.5, used the "sandwich" configuration as shown in Figure 2.2 B.

The temperature was calculated at a series of times for each shot. We assumed a simple melting phase boundary and neglected the difference between solidus and liquidus. From these measurements we find that the melting point of SS is 5500 $\pm$ 250 K at 240 GPa. We see that there is a systematic difference between the shock temperatures for iron (reported in detail in Chapter 3) and those for SS which agree

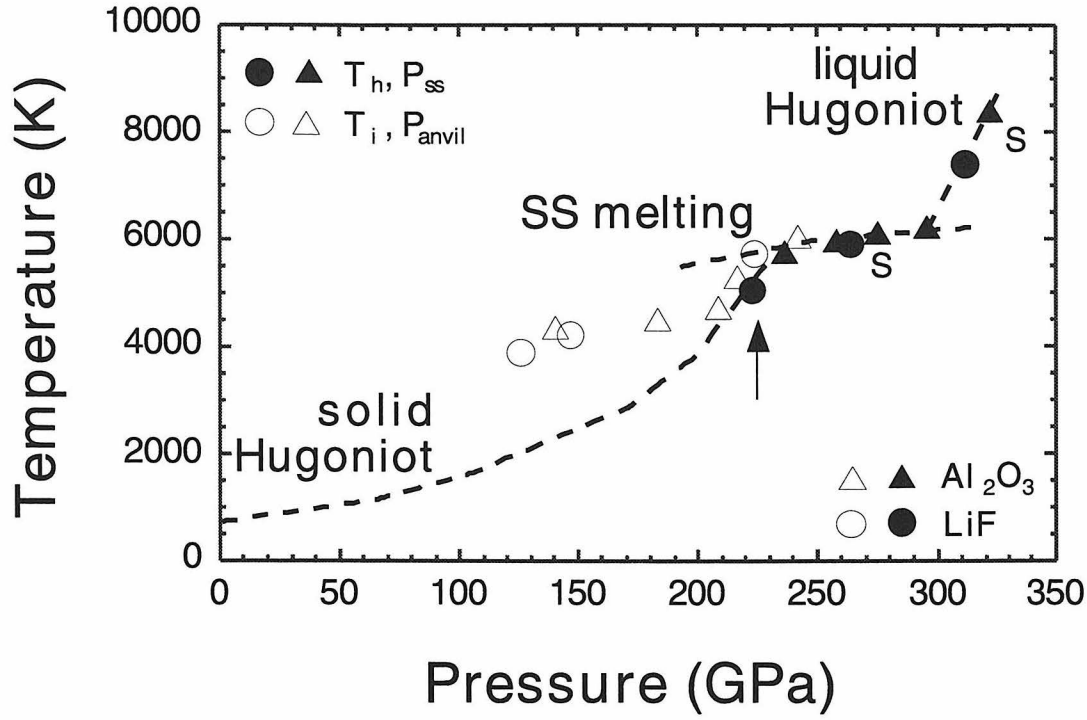

Figure 2.5: Hugoniot temperatures of stainless steel from Table 2.2. Open and solid symbols are observed interface temperatures, T_i, and inferred Hugoniot temperatures, $T_{h,m}$. Circles and triangles are data from LiF and Al_2O_3 anvils, respectively. The arrow represents the pressure at which Hixon et al. [1994] observed melting. The two points labeled "S" represent shots 271 and 278 in which the sandwich configuration was used.

with the calculations by McQueen et al. [1970] (see Figure 2.6). Additionally, the time dependence of interface temperatures for the "Sandwich" configuration experiments shows that T_i decreases by no more than 5 mv (or 50 K) in 250 ns (figure 2.7). The flatness of the radiation versus time curves for all pressures and film thicknesses and anvil materials implies that the LiF and Al_2O_3 anvils are not becoming measurably opaque under shock loading to 140 and 240 GPa respectively.

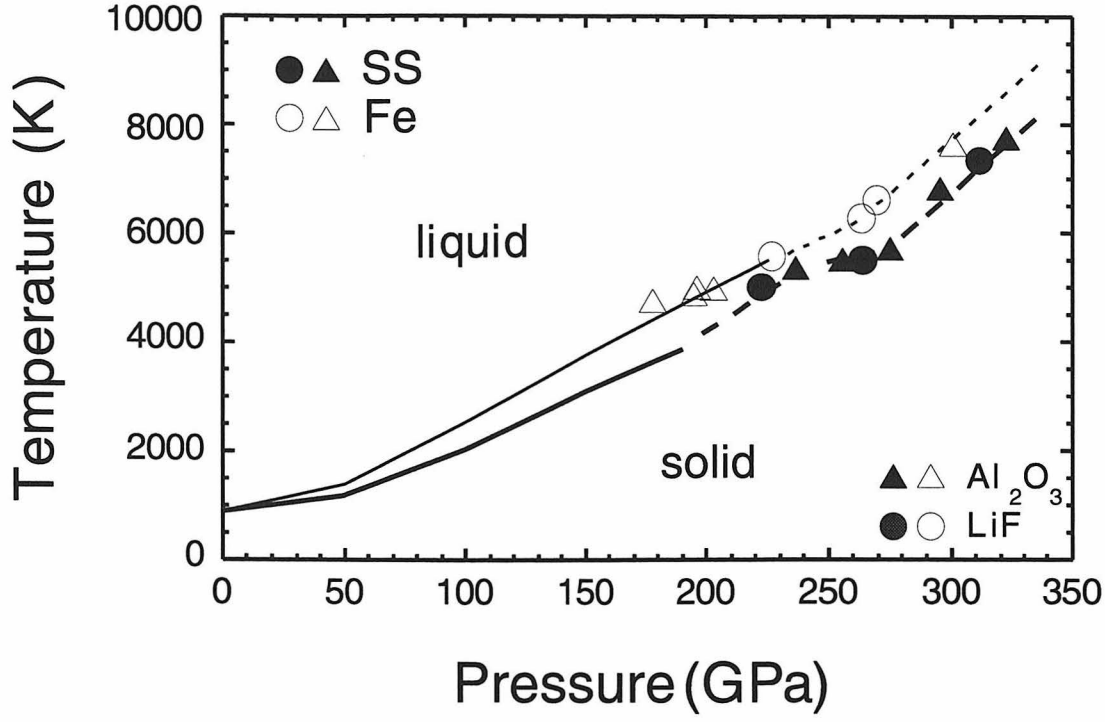

Figure 2.6: Comparison of the shock temperatures of iron and stainless steel. Open symbols are data for iron (shots 168, 159, 190, 189, 304, 307, 287, 289, see Chapter 3), solid symbols are for stainless steel (Table 2.2). Circles are for LiF and triangles are for Al_2O_3 anvils.

2.5 Calculations

We can also show that heat is not diffusing out of the thin films and into the Al_2O_3 anvils at a rate fast enough to cause a measurable temperature decrease. The heat conduction can be modeled by a symmetric boundary value problem with the ordinary one-dimensional heat flow equation:

$$\frac{d^2T}{dx^2} = \frac{1}{\kappa}\frac{dT}{dt} \ . \tag{2.2}$$

Here, T is the temperature of the medium at position x and time t, while κ is the thermal diffusivity. The initial temperature distribution is shown in Figure 2.8, labeled as 0.0 and is described by the equations (2.3) and (2.4).

$$T(t = 0, |x| < a) = T_1 \tag{2.3}$$

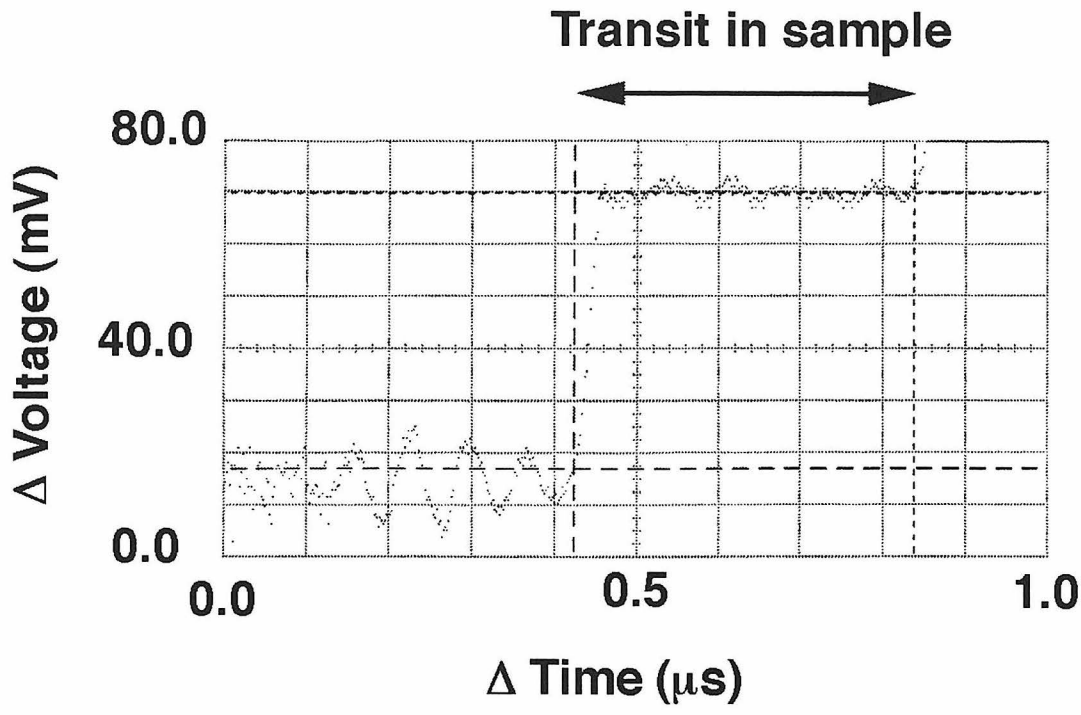

Figure 2.7: Time dependence of interface radiation from sandwich configuration with 1 μm SS, shot # 271, $\lambda = 600nm$.

$$T(t = 0, |x| > a) = 0 \ , \tag{2.4}$$

where a is half the thickness of the stainless steel film. As a first approximation, the case is studied where the diffusivities of the three regions are held to be that of the anvil material $\kappa_{\text{driver}} = \kappa_{\text{film}} = \kappa_{\text{anvil}}$. This approximation allows an analytic solution to the problem [Carslaw and Jaeger, 1993, page 54].

$$T = T_o + \frac{1}{2} T_1 \left\{ erf[\frac{a - x}{2\sqrt{\kappa_1 t}}] + erf[\frac{a + x}{2\sqrt{\kappa_1 t}}] \right\} \tag{2.5}$$

Equation 2.5 only provides a lower bound to the solution of the heat flow in our experiment, because the anvil diffusivity should be much lower than that of the metal, by a factor of 10^3. The solution to the case where the center region has a different diffusivity than the outer regions is more difficult and is discussed in detail in the Appendix A of this thesis, and implemented in Chapter 3.

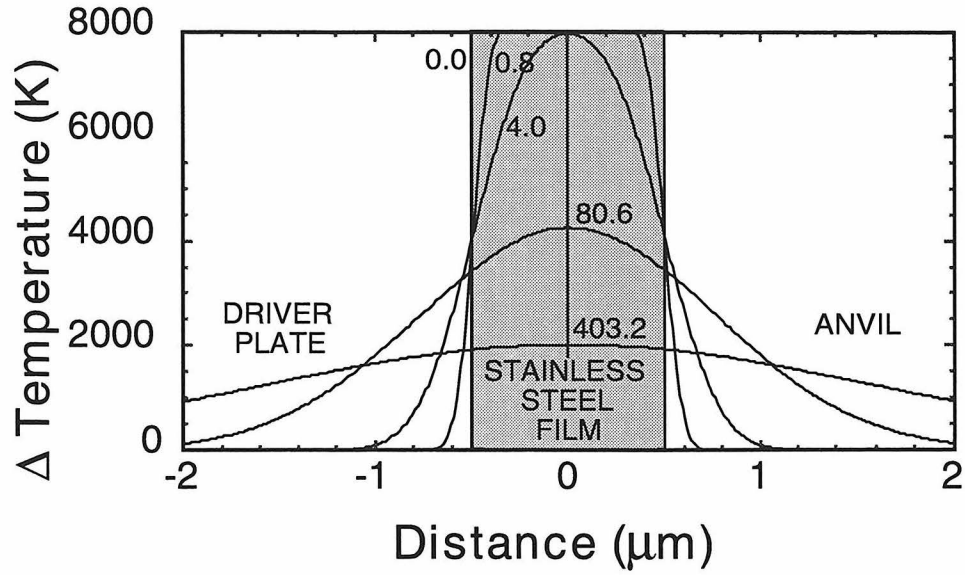

Figure 2.8: Analytical model of heat flow (Eq. 2.5) assuming constant thermal diffusivity and the thin film "sandwich" experimental configuration. Temperatures cooled from an initial temperature distribution, at t_0 to distributions shown for given times (ns).

Figure 2.8 shows that in order to get a 50 K decrease, which is the smallest resolvable, we would require a time of ~50 ns, which is 5 times shorter than the 250 ns time of our experiments. Since we did not see this temperature decrease in Figure 2.7 we can use this information to calculate an upper bound to the thermal diffusivity of the anvil, κ_a:

$$\kappa_a = k_a/\rho_a C_{p_a} \leq 14 \pm 5 \text{ cm}^2/\text{s} . \tag{2.6}$$

Here, ρ_a, C_{p_a}, and k_a are the density, heat capacity, and thermal conductivity of the anvil. Since k_a is the least well constrained of the three variables, we can assume that the major uncertainty is due to inadequate knowledge of k_a. We thus calculate that $k_a \leq 15 \pm 2$ W/m·K for Al_2O_3 at 241 GPa . This value is 1.6 times lower than that predicted by the method of Tan and Ahrens [1990] in Bass et al. [1987]. We calculate Hugoniot temperatures for our data set. For example, upon making this correction in the calculated value for $T_{h,m}$ in shot 270, we obtain a revised value of 6247 K, which is ~ 300 K less than the value previously calculated.

2.6 Conclusion

For a 1 μm stainless steel film shocked up to 321 GPa in the sandwich configuration (with anvil pressure of 241 GPa), the best fit temperature at the interface decreases by no more than 50 K after 250 ns. The constancy of the radiation intensity with time implies that Al_2O_3 shocked to 241 GPa is not measurably absorptive. Within the errors of the measurement, enough heat does not conduct out of the film into the Al_2O_3 to create a measurable temperature difference at the interface. Since the diffusivity of Al_2O_3 is much less than that of SS, Al_2O_3 limits heat conduction at the interface. Thus we may apply our simple model of the sandwich configuration to determine that the diffusivity of Al_2O_3 is ≤ 14 cm^2/s at 208 GPa and $T_i = 4739$ K. This is a factor of 1.6 lower than the calculated value of Bass et al. [1987] and yields a Hugoniot temperature of 6160 K.

We measured shock temperatures of stainless steel and using our values for thermal diffusivity ratio, calculated Hugoniot temperatures of 5000 - 8500 K in the pressure range 222 - 321 GPa. The melting temperature was 5500 K $\pm$ 250 K at 241 GPa SS pressure, and the shock temperatures were independent of the anvil material (LiF or Al_2O_3) as well as consistent with each other. Moreover, theoretically and experimentally there was a systematic difference between $T_{h,m}$ data for iron and for stainless steel films ranging from 300 K at 222 GPa to 700 K at 321 GPa SS pressure. This difference is consistent with the temperature difference calculated by McQueen et al. [1970].

Chapter 3

Transparency and thermal conductivity of LiF and Al_2O_3 to 240 GPa

3.1 Introduction

The phase diagram and thermal properties of iron and its alloys at ultra-high pressures are important because they provide vital information for understanding the Earth's core, and also because they add to the fundamental understanding of the behavior of materials at high pressure. However, experimental determination of these properties is difficult. Dynamic and static experiments each have their own challenges [Gallagher et al., 1994; Boehler, 1994; Jeanloz and Ahrens, 1977; Yoo et al., 1993] and the results in the 50 - 200 GPa range have previously been disparate. Not only does the extrapolation of static results to higher pressure disagree with the higher pressure dynamic results, but some static experiments conducted at different laboratories do not agree with each other.

Shock temperature experiments require spectral measurements of Planck radiation from the sample. Shock temperature determinations on opaque materials such as iron are difficult because one cannot directly observe the interior of the shocked material. It is therefore necessary to employ a transparent anvil material which maintains pressure on the surface of the sample and permits observation of the high pressure metal/anvil interface, via transmission through the anvil. This method has inherent difficulties [Nellis and Yoo, 1990], the three most important of which are addressed here. First, the shock-compressed anvil materials must be sufficiently transparent so that radiation from the iron/anvil interface may be measured. Second, the reduction of interface temperature to the shock temperature in the interior of the sample requires knowledge of thermal parameters which are not easily measured at the conditions of the interface, specifically, thermal diffusivity, specific heat at constant pressure and compressed density. Third, imperfections at the iron-anvil interface can lead to local deposition of irreversible work, and hence induce anomalously high temperatures.

When a shock wave propagates from one material to another that is both in ideal contact and has a similar shock impedance, most of the energy of a shock wave is transmitted, rather than reflected. The optical properties of Al_2O_3, which has a similar shock impedance to iron and is used as an anvil material in shock temperature experiments of metals, have been controversial. Initially Grover and Urtiew [1974] inferred that Al_2O_3 became opaque above 85 GPa. However both Ahrens et al. [1990b] and McQueen and Isaak [1990] concluded that the Grover and Urtiew analysis was too simplified. A more detailed analysis demonstrated the transparency of Al_2O_3 to 200 GPa. Ahrens et al. [1990b] and Williams et al. [1987] assumed that spectroscopic grade Al_2O_3 remained transparent while in the shocked state, implying that the anvil material is indeed a good window material and that one can observe optical radiation from the metal at the anvil/metal interface. In contrast, Kondo [1994] conducted experiments up to 80 GPa on single crystal Al_2O_3 and concluded that it becomes opaque under shock loading

and suggested that the radiation in shock temperature experiments on metals [Williams et al., 1987; Bass et al., 1987; Ahrens et al., 1990b] originates from the anvil, not the metal. Thus Kondo claimed that in the shock temperature experiments on metals these authors measured the temperature of the Al_2O_3 anvil rather than that of the metal. Additionally, Funamori and Jeanloz [1997] measured a phase transition in Cr^{3+} doped Al_2O_3 using a heated diamond anvil cell above 100 GPa. They suggest that this phase transition may affect the interpretations of shock experiments, but it is not obvious whether the phase transition occurs under shock loading, or exactly how it affects the optical properties of Al_2O_3. How radiation from the metal can be distinguished from anvil radiation during a shock temperature experiment is germane, especially in view of the above results by Kondo with Ag films deposited on Al_2O_3 and by Funamori and Jeanloz in the diamond anvil cell. In the present paper we address this issue by studying the systematic differences in the radiation observed from sample assemblies in different experiments. For example, if observed interface temperature varies systematically with the type of metal sample used, but not with the type of anvil, then the optical radiation is inferred to originate from the metal/anvil interface, and therefore reflect the properties of the metal and anvil, rather than just the anvil.

One of the critical parameters used to calculate Hugoniot temperature from interface temperature is the thermal diffusivity ratio between the metal and the anvil, R. We carried out a series of experiments (discussed in the Section 3.3.2) to measure this parameter. Due to the fact that the surface roughness of the anvil is on the order of the same thickness of the films, the "thin film" experiments do not provide accurate shock temperature data for iron. Therefore results from other experiments (discussed Section 3.3.1) are analyzed using R values determined in "thin film" experiments. Revised Hugoniot temperatures for Fe are reported. These results do not by themselves yield a pressure where the iron Hugoniot intersects the solid-liquid phase boundary. However, Brown and McQueen [1986] observed a drop in sound velocity that they inferred corre-

sponded to the onset of melting at 243 ± 3 GPa along the principal Hugoniot of iron. We have thus interpolated our temperature results to infer melting at 5860 ± 390 K and 243 GPa.

In the present paper we use the lack of correlation of shock temperature with anvil material to address the origin of the optical radiation during shock temperature experiments on iron. We then discuss the data reduction of these experiments and later experiments to determine R. We also discuss issues related to effects and problems at the iron/anvil interfaces. Finally, we determine a revised phase diagram for iron that predicts a temperature for the onset of melting of an assumed hexagonal closed packed phase, possibly the epsilon or a similar structure, along the principal Hugoniot.

3.2 Relevant equations

We drive a shock wave into the metal sample inducing a Hugoniot pressure, $P_{h,m}$, volume, $V_{h,m}$, and temperature, $T_{h,m}$. Upon reflection at the anvil, a release wave is reflected back into sample, resulting in a release-pressure $P_{r,m}$ and release-density $\rho_{r,m}$ in the metal. The temperature of the interface between the anvil and the metal, T_i, is observed. In the present case we assume the anvil has a slightly lower shock impedance than the metal sample [Ahrens, 1987].

The temperature of the interior of the released metal sample [Grover and Urtiew, 1974], $T_{r,m}$, is calculated from T_i via:

$$T_i = T_{r,m} - \frac{T_{r,m} - T_{h,a}}{1+\alpha} \ , \tag{3.1}$$

where $T_{h,a}$ is the internal shock temperature of the anvil, and α is defined by:

$$\alpha = \sqrt{\frac{k_m \rho_m C_{Pm}}{k_a \rho_a C_{p_a}}} \ . \tag{3.2}$$

Here, the specific heat at constant pressure, C_p, is defined by

$$C_p = C_v(1 + \gamma \alpha^{th} T) \ , \tag{3.3}$$

ρ is the high-pressure density, k is the thermal conductivity at high pressure and temperature, and $C_v = 3R_u/w$ is the specific heat at constant volume, where $R_u = 8.31441$ J/K·mol is the universal gas constant, and w is the mean atomic weight at P_r and T_i. The subscript 'a' denotes the anvil material and the subscript 'm' denotes the metal. Previous authors [Ahrens et al., 1990b] have used C_v instead of C_p in Eq. 3.2; this makes only a 0.4% difference in the resulting value for α. The values of the thermal parameters used here are shown in Table 3.1. The coefficient of thermal expansion [Duffy, 1993] can be estimated as

$$\alpha^{th} = \frac{\rho_0 \gamma_o C_v}{K_T} (\frac{\rho_0}{\rho_r})^{q-1} , \tag{3.4}$$

where ρ_0 and ρ_r are the initial and compressed densities of the material, q is dimensionless parameter often taken to be $q = 1$, and K_T is the isothermal bulk modulus at P_r and T_i. Ahrens et al. [1990b] also estimated k_a at zero and high pressure (0 and P) at temperature T from:

$$k_a(T, 0) = A + B/T \tag{3.5}$$

$$k_a(T, P) = k_a(T, 0) \left(\frac{\rho_r}{\rho_0}\right)^{2\gamma+5/3} , \tag{3.6}$$

where $A_{Al_2O_3} = -2.599$ W/mK, $B_{Al_2O_3} = 1.176 \times 10^4$ W/m, $A_{LiF} = -0.2$ W/mK, and $B_{LiF} = 3.7 \times 10^3$ W/m are measured at ambient pressure and high temperature and γ is the Grüneisen parameter. Other formulations [Tang, 1994; Leibfried and Schlömann, 1954] calculate $k_a(T, 0)$ analytically and produce similar results in the temperature range of interest. Eq. 3.6 results from the approximate formula $\frac{\delta \ln \kappa}{\delta \ln \rho} = 2\gamma + 5/3$ and the assumption $\gamma = \gamma_0$. Without this assumption, a lower value of $k_a(T, P)$ would be predicted. Hofmeister [1999] calculates $k_a(T, P)$ based on phonon lifetimes, lattice mode vibrations, conduction and transport via blackbody radiation, producing conductivities that are lower than from Equation 3.6 by as much as a factor of two for olivine. However

Table 3.1: Calculated properties along the Hugoniot of Al_2O_3 and LiF (denoted 'A' and 'L'). V_{impact} is the impact velocity of the experiment, γ is calculated from $\rho\gamma$ =const. The thermal expansion coefficient, α^{th} is calculated from Equation 3.4, and C_p is from Equation 3.3.

Shot #	anvil mat.	$T_{h,a}$ calc. (K)	$P_{h,a}$ calc. (GPa)	$\rho_{h,a}$ calc. (gr/cc)	γ grun.	α^{th} calc. (10^{-6}/K)	C_p anvil (J/kg · K)	K_T anvil (GPa)
285	A	2747	244	6.17	0.85	1.18	1720	510.9
286	L	4217	166	4.62	1.00	2.00	1940	257.8
287	L	4186	164	4.61	1.00	2.10	1940	256.3
296	A	1412	165	5.58	0.94	1.67	1780	398.8
297	A	1406	164	5.58	0.94	1.68	1780	386.2

we use Equation 3.6 to facilitate a direct comparison of our $T_{h,m}$ values with the results of Ahrens et al. [1990b].

Fourier conduction of heat from a high temperature metal film into a lower temperature anvil material is dependent upon the thermal diffusivity ratio, R.

$$R = \frac{\kappa_m}{\kappa_a} , \tag{3.7}$$

where κ_m and κ_a are the thermal diffusivities of the metal and the anvil material respectively. Thermal diffusivity, κ, is related to thermal conductivity, k, via

$$\kappa = k/\rho C_p , \tag{3.8}$$

where C_p is the specific heat at constant pressure and ρ is the high pressure density. The thermal conductivity of the metal, k_m, is calculated from the Wiedemann-Franz law:

$$k_m = L\sigma T , \tag{3.9}$$

where $L = 2.45 \times 10^{-8}$ W$\cdot\Omega$/K^2 is the Lorenz number, σ is the electrical conductivity of the metal, and T is the temperature. This formulation assumes that electrons transport the heat and that electron–phonon scattering dominates. This assumption is supported by the k_m data for iron of Secco and Schloessin [1989]. Manga and Jeanloz [1996] compared Secco's data to the electrical conductivity versus Hugoniot pressure data for iron of Matassov [1977] (see Chapter 2 of this thesis, Figure 2.3), concluding that the Wiedemann-Franz law was valid for Fe. Note that σ has a $1/T$ dependence and also a pressure, P, dependence, making Eq. 3.9 more properly $k_m(P) = L\sigma(P, 1/T)T$. Thus when calculating k_m for a thin film experiment which has a different shock temperature than the Hugoniot temperature of Fe, one must use a calculated reverberated shock temperature in Eq. 3.9, rather than a principal Hugoniot temperature, because that is the temperature at which the measurement of σ was made [Manga and Jeanloz, 1996].

To determine a Hugoniot temperature for an experiment employing a 'thick film' ($\geq$ 1 μm) an R value is used to calculate k_m/k_a via Eq. 3.7 and Eq. 3.8. The ratio k_m/k_a is then used to calculate α via Eq. 3.2, and α is used to calculate $T_{r,m}$ via Eq. 3.1. $T_{h,m}$ is calculated from $T_{r,m}$ via:

$$T_{h,m} = T_{r,m} \exp\left[\gamma_o \rho_o \frac{(u_r - u_h)^2}{P_{h,m} - P_{r,m}}\right] , \tag{3.10}$$

where u_r and u_h are the release and Hugoniot particle velocities in the metal sample.

To determine the Hugoniot temperature for a "thin film" experiment, the pressure in the film is approximated by the Hugoniot pressure in the anvil, $P_{h,a}$. Equation 3.1 does not apply directly for "thin films", which cannot be approximated by an infinite half-space. The temperature achieved by the film can be approximated by

$$T_{h,m} = T_{r,m} + \exp\left[\int_{V_{r,m}}^{V_{h,m}} \frac{\gamma}{V_m} dV_m\right] . \tag{3.11}$$

where $T_{r,m}$ is given Equation 3.1 and the second term approximates the shock reverberation in the film with adiabatic compression from state $P_{r,m}$, $V_{r,m}$ to final state P_{final},

V_{final}. We determined reverberated shock temperatures, $T_{r,m}$, for the experiments employing "thin films" ($\leq$ 1000 Å) by comparing the measured T_i and the calculated $T_{h,a}$ to a scaled finite element model (see the appendix of this thesis, Chapter 5) for symmetric heat flow from a thin film; Eq. 3.10 is used to calculate $T_{h,m}$ from $T_{r,m}$.

3.3 Shock temperature experiments on metals

The shock temperature experiments on metals were performed on a 2-stage light-gas gun [Ahrens, 1987] via optical pyrometery [Yang, 1996]. There are two different types of sample configurations used, the "thick film" setup, using 1 μm or thicker films and the "thin film" experiments using 200, 500, or 1000 Å films. In both cases, the metal film is in contact with the anvil materials that serve to compress the metal at high pressure. The Al_2O_3 used for our experiments was obtained from the Adolph Mueller Company, as spectral grade sapphire, and the LiF was obtained from Bicron Inc., as optical grade windows. The metal surface is intended to be viewed through one of the transparent anvils during the time the shock wave passes through the anvil.

To address the issue of interface quality, we grew films from 99.995% purity iron targets epitaxially on our anvil materials using argon ion sputtering in ultra high vacuum 5×10^{-9} torr. We used the resulting samples for both the "thick film" experiments reported in Section 3.3.1, and for "thin film" thermal diffusivity experiments reported in Section 3.3.2. The 1000 Å film that was used for Shot #287 was deposited in 40 minutes on a 500^o C preheated LiF substrate, and a shallow angled electron scattering pattern (RHEED) was observed in situ to show that the deposited film displayed limited long-range order [Hashim at al., 1993]. An SEM image (Figure 3.1) was obtained to demonstrate that there was no micron scale porosity. The image shows no dark patches in the uppermost light grey area, which would imply that there was measurable porosity. Additionally the image shows clearly that the length-scale of surface roughness of the

A)

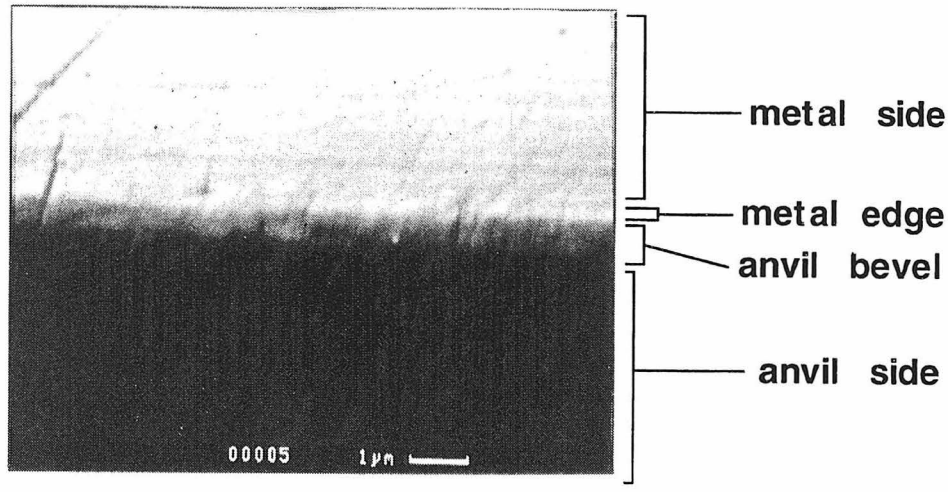

B)

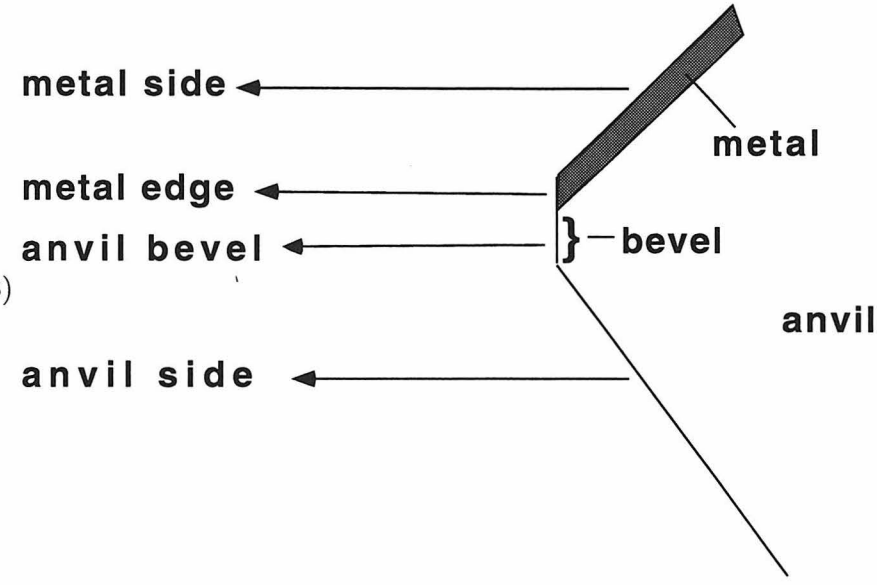

Figure 3.1: Scanning electron microscope (SEM) image of the 1000 Å Fe film used in Shot #297. The film is shown as deposited upon the Al_2O_3 anvil, tilted at a 45 deg angle to the SEM. The dark lower section is the anvil, and the lighter section in the middle is the bevel at the edge of the anvil. The very thin pale line above the bevel is the edge of the Fe film, and the medium grey section at the top is the face of the Fe film, with the Al_2O_3 visible through the Fe.

anvil is much larger than the thickness of the metal film, which is the thin pale line in the center of the figure. This leads to an effective porosity in the film, which results in "thin films" having anomalously high shock temperatures.

3.3.1 Thick film experiments

The target configuration for a "thick film" shock temperature experiment is given in Figure 3.2. The flyer plate travels though a vacuum $\leq 4.2 \times 10^{-5}$ bar and impacts the metal driver plate, which is (with the exception of one experiment) of the same type material as the metal film. The light emitted from the film/anvil interface is masked so as to block light emitted from portions of the sample that have been affected by shock wave reflections from the edges of the anvil. Epoxy holds the driver plate to the edges of the anvil/film assemblage, but no epoxy is placed between the film and the driver. Because metal thickness (film plus driver) is much greater than thermal skin depth, the metal-anvil interface temperature does not change during the experiment even though heat flows across the metal-anvil interface [Grover and Urtiew, 1974].

Previous shock temperature experiments [Ahrens et al., 1990b; Tan and Ahrens, 1990; Yoo et al., 1993], on metals have employed thick films or foils. In these cases the metal/anvil interface can be modeled as two infinite half-spaces in contact. Specifically, a "thick film" is one where the thickness is much greater than the thermal skin depth. The opacity and emissivity of the high pressure anvil material is not well constrained in any previous experiment and one cannot determine directly from a single experiment whether the metal/anvil interface or the bulk material of the anvil is the source of the spectral radiation, however one can determine the source of the radiation and thus constrain the emissivity and opacity of the high pressure anvil material by systematically examining the data from sets of "thick film" experiments. Thick film shock temperatures show systematic temperature differences that depend on the film material used

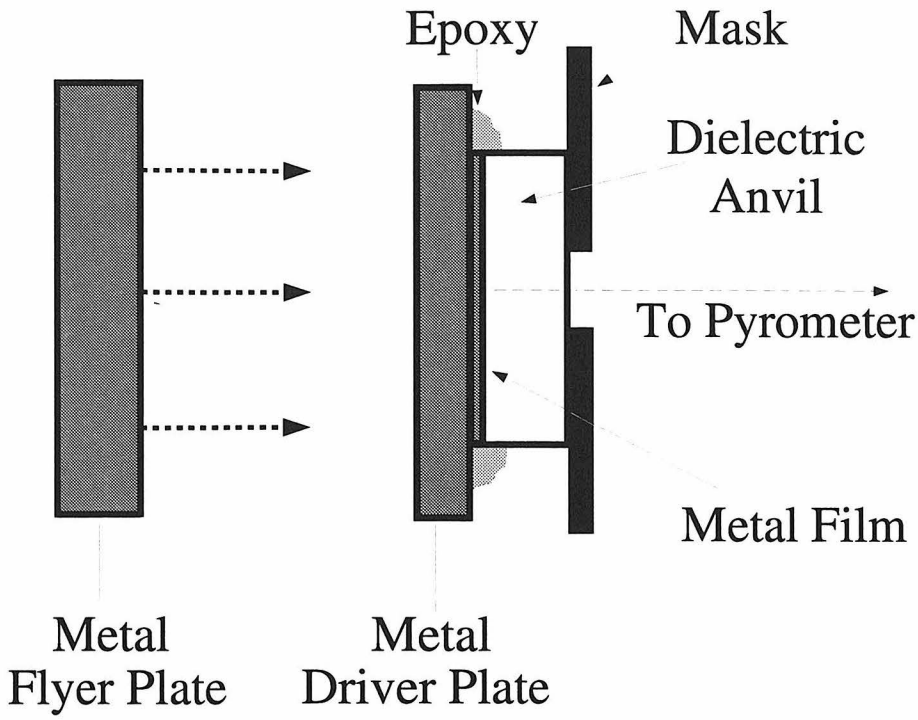

Figure 3.2: Thick film target configuration. The metal film and the driver are of the same material. At a series of wavelengths described in Table 3.4, optical radiation from the metal/anvil interface is detected by a pyrometer and recorded at 1 ns intervals during the approximately 300 ns shock transit time in the anvil.

but not the anvil material. In Chapter 2 of this thesis, Figure 2.6 showed the results of experiments on Fe and stainless steel (SS), using both LiF and Al_2O_3 anvils. At a given pressure the Hugoniot temperatures measured for SS films are consistently lower than for Fe films, as expected theoretically [McQueen et al., 1970]. There is no significant systematic difference in the temperature achieved with different anvil materials. This result is difficult to reconcile if the radiation originates within the anvil, but it is consistent with the thermal radiation originating at the metal-anvil interface. This is the first of several pieces of evidence supporting the transparency of Al_2O_3 (and LiF) during our experiments.

Table 3.2 shows the thermal parameters that were used in the data reduction of the shock temperature experiments on iron which are shown in Figure 2.6 and which are

also discussed in terms of the phase diagram of iron in Section 3.5. Shots 304 and 307, represent new iron shock temperature data.

Table 3.2: Thermal properties of iron used in reducing shock temperature experiments. The first four entries are previous experiments reported in Ahrens et al. [1990b] and new experiments reported in this work are shots 304 and 307. Electrical conductivity of the metal sample, σ_{elect} is extrapolated from Matassov [1977] (Figure 2.3), thermal conductivity, k_m, is from Equation 3.9. Release temperature calculated from Equation 3.1. Hugoniot temperature, $T_{h,m}$, is calculated from Equation 3.10, and compared with the previously reported temperatures in Ahrens et al. [1990b]. In all cases the driver plate is Fe. Window materials Al_2O_3 and LiF are denoted 'A' and 'L'

Shot	$P_{h,m}$	flyer	Win.	V_{impact}	ρ	T_i	σ_{elect}	k_m	κ_m	$T_{h,m}$	$T_{h,m}$
#	Fe	mat.	mat.	exp.	Fe	exp.	10^6	therm.	10^{-6}	calc.	prev
	(GPa)			(km/s)	(gr/cc)	(K)	(1/Ω·m)	(W/m·K)	(m^2/s)	(K)	(K)
168	300	Ta	A	6.00	11.98	6990	0.777	179.5	31.56	7598	8930
159	263	Ta	L	5.06	11.81	5270	0.813	156.5	28.07	6270	7240
190	227	Ta	L	5.09	11.61	4660	0.850	133.1	24.77	5560	6180
189	202	Ta	A	5.52	11.46	4010	0.876	116.5	21.83	4910	5200
304	194	Ta	A	4.88	11.90	4814	0.884	111.2	20.88	4901	–
307	178	Cu	A	5.32	11.30	4557	0.902	100.4	18.85	4822	–

3.3.2 Thin film experiments

A series of shock temperature measurements were performed on thin iron films, sandwiched between two dielectric anvils (Figure 3.3). For the duration of the experiment, there is symmetric heat flow from the iron into the anvils. As shown in Table 3.3, calculated shock temperatures are significantly lower for dielectric anvils than for metal films ($T_{h,a} < T_{r,m}$). When the film is thin, the interface temperature decays with time

Table 3.3: Experimental and theoretical high temperature and pressure thermal conductivities, $k_a(T,P)$, and diffusivity ratios, R, of corundum (Al_2O_3) and griceite (LiF). The optical pyrometer which measured the temperature of the interface between the metal and the anvil, T_i had six channels but for two experiments (shots 285 and 297) an entire channel was not used because the data was off scale, leaving five usable channels. Additional thermodynamic parameters used to calculate the thermal conductivity of the anvil materials, $k_a(T,P)$, are given in Table 3.1.

Shot	2a	Anvil	$P_{h,a}$	$P_{h,m}$	$T_{h,a}$	$T_{r,m}$	T_i	ΔT_i	$k_a(T,P)$	$k_a(T,P)$	$\Delta k_a(T,P)$	$\kappa_a(T,P)$	$\kappa_m(T,P)$	R	R	ΔR
#	Å	mat.	(GPa)	(GPa)	(K)	(K)	(K)	(±K)	$(\frac{W}{mK})$	$(\frac{W}{mK})$	$(\frac{W}{mK})$	(mm^2/s)	(mm^2/s)	Fe/anvil	Fe/anvil	(±)
	Fe		anvil	iron	anvil	iron	interf.	interf.	calc.	fit	fit	calc.	calc.	calc.	fit	fit
285	500	Al_2O_3	244	303	2747	9548	11000	120	16.5	6	2	1.56	109.7	70.5	80	20
286	500	LiF	166	261	4217	7763	8300	490	8.57	2.3	1	0.96	27.8	29.1	35	15
287	1000	LiF	164	269	4186	7665	7550	520	12.6	3.4	1	1.41	161.1	11.4	15	30
296	500	Al_2O_3	165	197	1412	5226	7090	1140	33.3	12	3	3.35	211.6	62.9	70	11
297	1000	Al_2O_3	164	196	1406	5203	6451	1030	33.4	12	3	3.36	210.9	62.7	72	21

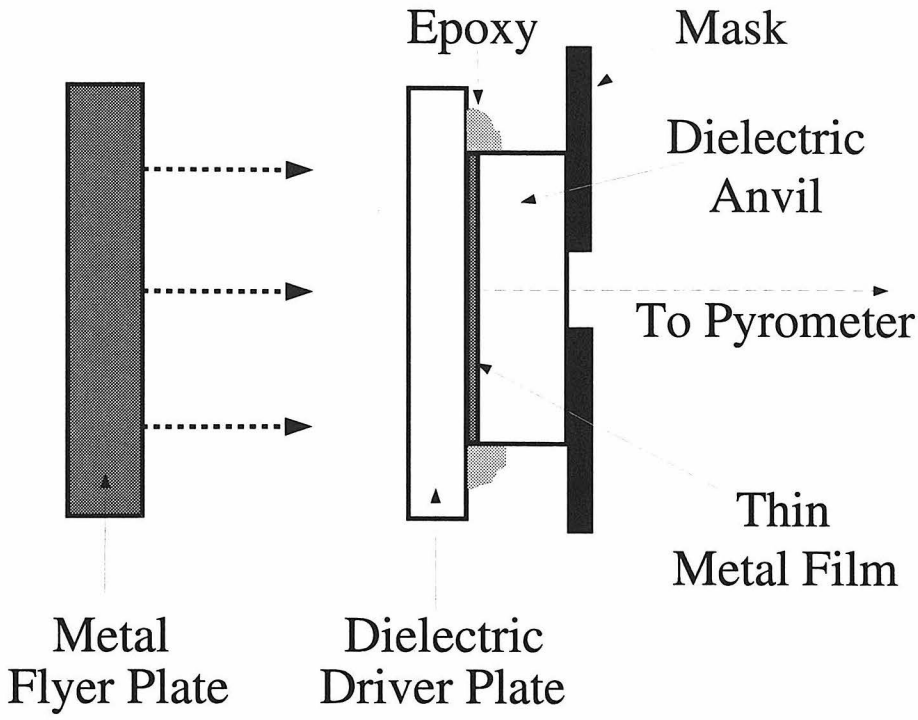

Figure 3.3: Thin film target configuration. The anvil and the driver are of the same material. At a series of wavelengths described in Table 3.4, optical radiation from the metal/anvil interface is detected by pyrometery and recorded at 1 ns intervals on a digitizer during the $\sim$ 300 ns shock transit time in the anvil.

as heat flows across the boundary. We observed this decay and fit it to a finite element one-dimensional heat flow model (see the appendix of this thesis, Chapter 5 for details) to obtain thermal diffusivity ratios, R (defined by Equation 3.7), for the experimental materials (Figure 3.4). Table 3.3 shows the best fit R values, and corrects values given previously [Gallagher and Ahrens, 1996]. In the table, 2a is the thickness of the thin iron film undergoing symmetric heat flow, $P_{h,m}$ is the Hugoniot pressure of the iron or of the anvil material during the experiment. $T_{r,m}$ is the calculated release temperature of the iron or of the anvil material at the given $P_{h,m}$. T_i is the interface temperature measured during the experiment. ΔT_i is the RMS error in the grey body fit to temperature after time averaging. $k_a(T,P)$ is the thermal conductivity of the anvil material; both theoretical values (Equation 3.6), and experimentally inferred values are listed.

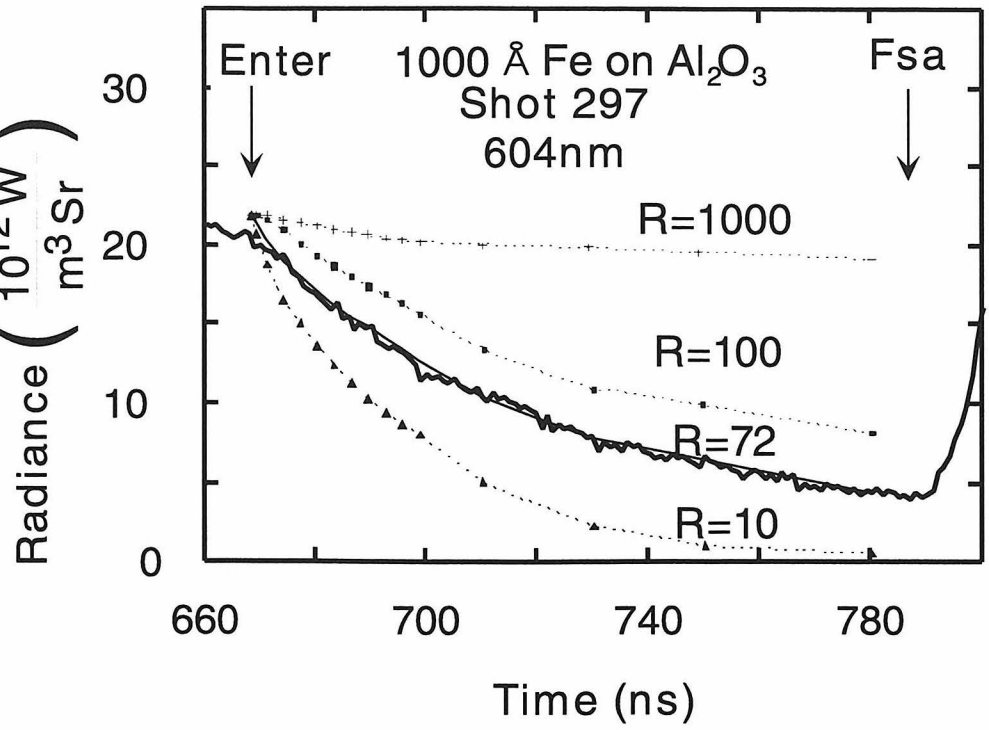

Figure 3.4: Time dependent interface radiance for 1000 Å Fe on Al_2O_3 Shot # 297, pyrometer channel # 3, 603.7 nm filter (center wavelength). Thermal decay models curves for diffusivity ratios R=1, 10, and 100 are shown scaled to the parameters of the experiment, as well as the model curve for the best determination R=72 for this time and wavelength. For details of the model calculations, see the Appendix A of this thesis.

R is the thermal diffusivity ratio (Equation 3.7), and calculated values, as well as ones experimentally determined by the decay of T_i during the experiment are listed. $\kappa_a(T,P)$ and $\kappa_m(T,P)$ are the theoretical thermal diffusivities of the anvil material and the metal sample, respectively. The detailed numerical procedure which was used to obtain experimental values for R, $k_a(T,P)$, ΔR and $\Delta k_a(T,P)$ is explained in the appendix of this chapter, Section 3.7.

One of the inherent difficulties in our method of observing shock temperatures of opaque metals is the possibility that calculated conductivity values, used to calculate Hugoniot temperatures from interface temperatures via Equation 3.1, may be inaccurate. As pointed out by Hofmeister [1999], such models overpredict pressure dependence

by as much as 50 to 100%. Our experiments provide data for R, the thermal diffusivity ratio, which is related via Equation 3.8 to the thermal conductivity ratio needed to calculate α (Equation 3.2). However it appears that the experimental values of R are slightly higher on average, but within errors, the same as previously calculated values by $10\pm15\%$ for Al_2O_3 and $17\pm43\%$ for LiF. The use of the "fit" $k_a(T,P)$ of Table 3.3 rather than values calculated via Equation 3.6 decreases the inferred Hugoniot temperature by about 350 ± 530 K. In light of this, the theory for thermal conductivities of insulating materials by Hofmeister [1999], which predicts lower values of $k_a(T,P)$, would be better to use than Equation 3.6, for future analyses of shock temperature data. There is no reason why the disagreement between experimental values and calculated values should disagree more for $k_a(T,P)$ than for R, so we assume the relatively good agreement for the R values is fortuitous.

The thin film experiments were intended to constrain the thermal diffusivity ratio of the metal/anvil interface, but can also be used to address the question of the source of the radiation. The systematics are consistent with the thick film experiments, in that no difference is observed between Hugoniot temperatures observed in experiments employing LiF and those employing Al_2O_3 anvils. Additionally, we observe a signal in which temperature decays with time, with the rate of decay depending on the thickness of the film. Thinner films (200 and 500 Å) decay faster than thicker films (1000 Å). Furthermore, since R for Fe/Al_2O_3 is higheer than R for Fe/LiF, a 500 Å film on Al_2O_3 should show a slower decay than a film of the same thickness on LiF (Figure 3.5). If anvil material were the source of the observed radiation, then the decay time should not depend on film thickness. Since $k_a(T,P)$ has a $1/T$ dependence, heat conducts faster at earlier times. Thus the slope flattens out after about 40 ns of heat conduction; this correspond to times labeled 450 ns on Figure 3.5. To facilitate the comparison between the two materials the temperatures plotted for shot # 296 (solid squares, Al_2O_3) have been linearly scaled to the temperatures of shot # 286 (solid circles, LiF). For shot #

286, the initial interface temperature $T_{i,m}$ = 8300 K and anvil Hugoniot temperature $T_{h,a}$ = 4217 K. For shot # 296 is $T_{i,m}$ = 7090 K and $T_{h,a}$ = 1412 K.

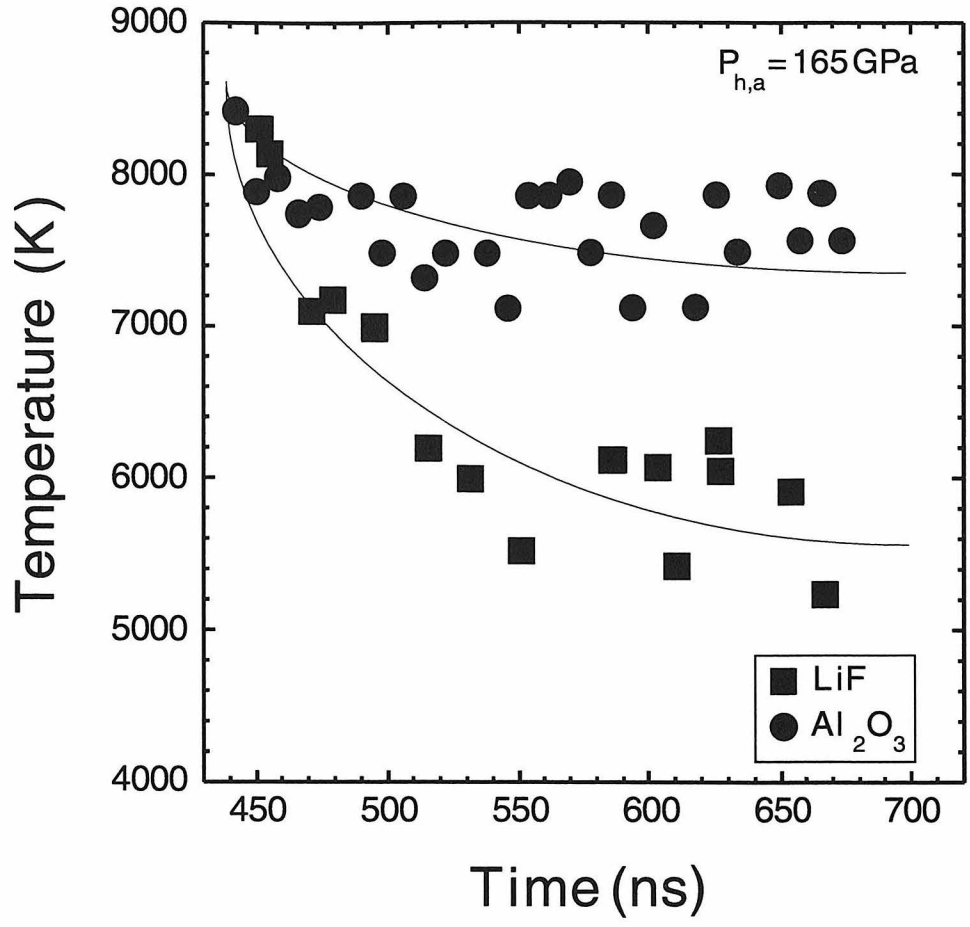

Figure 3.5: Comparison of conduction between Fe and LiF (solid squares, Shot #286, $P_{h,m}$=261 GPa, $P_{h,a}$=166 GPa), and between Fe and Al_2O_3 (solid circles, Shot #296, $P_{h,m}$=197 GPa, $P_{h,a}$=164 GPa). Interface temperatures decrease as heat conducts from the 500 Å Fe films into the anvils.

In our thin film experiments the temperatures decay while emissivities remain approximately constant, giving an overall decrease in radiation with time. If the source of the radiation had been the anvil, then the effective observed emissivity should have increased with time because as more of the anvil material enters the shock state, more of it would be radiating. This is one of several pieces of evidence supporting the transparency of Al_2O_3 during our experiments.

Tang et al. [1996] states that thermal contact resistance at the metal/anvil interface could be important in reducing shock temperature data. Because a contact resistance would allow a thermal boundary layer at the interface [Swarts and Pohl, 1989], Tang et al. interprets the initial high intensity that is seen in some experiments as being a measure of the temperature in the interior of the metal. We disagree with this interpretation for two reasons. First, for many of our best sample assemblies we see no initial flash. If the flash was caused by an intrinsic thermal contact resistance then it would be seen in all experiments, not just some. For this reason we prefer to explain the initial intensity of some samples as being a gap flash caused by an imperfect interface. Second, if Tang's interpretation is correct, we would expect the temperature of the initial flash to be consistent from experiment to experiment, but the observed grey body temperatures of the initial rises vary over a much wider range ($\pm$800 K) than the subsequent plateau temperatures ($\pm$250 K).

3.4 Radiation from anvil materials

The reason the radiating anvil material is not observed is related to the large differences in $T_{r,m}$ and $T_{h,a}$. There are two possible causes for radiation from the anvil, shear banding and grey-body emission from the continuum. If we were observing continuum anvil radiation, the amount of radiating material would increase with time (as the shock wave traverses the sample, it heats more and more of it), so the temperature would remain constant and the emissivity would increase with time. This would give an overall increase in photon flux with time. With a six channel pyrometer, we can resolve the emissivity time-dependence from the temperature time-dependence. In one experiment where the iron Hugoniot pressure was greater than 300 GPa (242 GPa in the Al_2O_3) this was observed, however it was not the case for the other experiments, and we have not seen this behavior with LiF. Thus the radiation is not originating from the

continuum of the anvil material for LiF and for Al_2O_3 below 242 GPa. If the radiation were caused by shear banding in the anvil material then, again, the amount of material involved in shear banding would increase with time, and the observed radiant intensity would increase with time. Additionally, shear banding dielectrics typically have very low emissivities $\epsilon \leq 10^{-2}$ [Kondo and Ahrens, 1983] whereas metals have emissivities in the range $0.1 \leq \epsilon \leq 1.0$. Our experiments show emissivities in the range 0.19 - 0.33. Therefore we conclude that for LiF and for Al_2O_3 below $\sim$ 240 GPa the radiation observed is from the iron and not the anvil. This is one of several pieces of evidence supporting the transparency of Al_2O_3 during our experiments.

As already stated, we did observe a single record that resembled Kondo's, where the Al_2O_3 Hugoniot pressure was $\sim$ 240 GPa. In this case, the radiation from the anvil material became brighter than the metal. Further we can distinguish between the two types of behaviors by examining the time dependence of emissivity. Kondo observes radiation from Al_2O_3 at Hugoniot pressures $<$ 80 GPa, below our experimental range. Moreover he is observing radiation from Al_2O_3 against a background radiation from Ag films that are 400 K hotter than those of iron at 90 GPa.

3.5 Discussion

One drawback of the thin film experiments is that in order for thermal decay to be observable on the $\sim$ 200 ns time-scale of our experiments, the film must be so thin as to be comparable to the surface roughness of the optically polished anvil materials and therefore comparable in thickness to the size of the gap between the driver and the metal-coated anvil. This causes the metal to achieve shock temperatures much higher than for thick iron films, 10,000 K as compared to 6000 K. The higher temperatures are useful in that they expedite heat flow during the experiments, but the state achieved is not representative of the ideal interface temperature and therefore is not a measurement

of Hugoniot temperature of iron. Thus, only thick film experiments can give reliable interface temperatures. We assume reliable Hugoniot temperatures can be calculated from "thick film" experiments by employing the thermal diffusivity ratios measured in the "thin film" experiments.

Figure 3.6 shows our two new thick film Hugoniot temperatures from shots 304 and 307, as well as reanalyzed Hugoniot temperatures for the experiments described in Ahrens et al. [1990b], and two Hugoniot temperatures we were able to obtain from the thickest of our "thin film" experiments, and also phase boundaries obtained from static experiments. Sound speed measurements by Brown and McQueen [1986] detect what they interpreted as the melting of ϵ-iron under Hugoniot conditions at 243 $\pm$ 2 GPa. These measurements are accurate for determining the pressure of melting, but the melting temperatures inferred from the experiments are calculated theoretically, and there is no direct evidence for which crystallographic phases are involved in the observed transition. In Figure 3.6 We interpret the two discontinuities in sound speed observed by Brown and McQueen [1986] as corresponding to the ϵ-γ and the proposed β-liquid iron transitions respectively. In this interpretation, the γ phase does not exist above 100 GPa and 3000 K [Chen, 1998]. Note that the thermal properties of β-iron are uncertain and need to be determined before a more accurate assessment of Hugoniot temperatures of can be made. We assumed the properties of ϵ-iron in our data analysis.

Hugoniot temperatures (and hence interface temperatures) versus pressure are expected to show a decrease in slope where the temperature of the solid first intersects the solid-liquid phase boundary, because the melting temperature decreases with pressure more slowly than the Hugoniot temperature. With increasing pressures, the shock temperature of the solid-liquid regime follows the solid-liquid phase boundary [Bass et al., 1987] and slope should increase again, following the liquid Hugoniot when complete melting has occurred. We refer to this behavior as an "offset" in the shock temperature

slope. This "offset" in our data, if present, is too small to be observed with present methods. Therefore the present data do not agree in detail with the phase boundary inferred by Yoo et al. [1993], who observed this expected effect at $\approx$ 250 GPa with shock temperature experiments on iron using diamond anvils.

Interpolation of our data to 243 GPa yields a temperature of 5860 $\pm$ 390 K. This

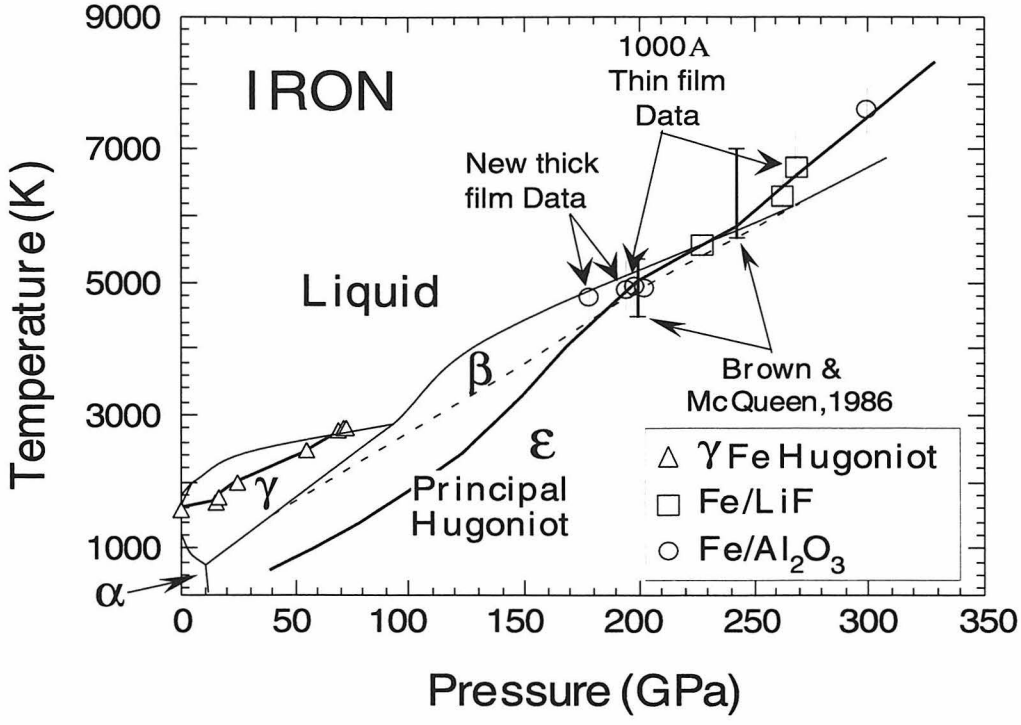

Figure 3.6: Hugoniot temperatures for Fe (heavy line). Data from thick film experiments (Table 3.2, shots 159, 168, 189, 190, 304 and 307) using R values determined from thin film experiments, and data from 1000 Å thin film experiments (Table 3.3, shots 287 and 297). Both Al_2O_3 (squares) and LiF (circles) anvils were used. Triangles represent dynamic experiments on the melting of γ-iron [Chen, 1998]. Medium lines represent phase boundaries determined from static measurements [Boehler, 1994; Yoo et el., 1995]. The dashed line represents the speculative ϵ to β phase boundary [Boehler, 1992]. The indicated uncertainty at 243 GPa was determined via sound speed measurements, assuming melting of ϵ-phase iron (a possibly incorrect assumption) [Brown and McQueen, 1986]. The principal Hugoniot temperatures at lower pressures are from Brown and McQueen's model b ($\gamma = 1.34$, $\frac{dE}{dP}|_v = 0.051$ m^3/Mg).

is within the error bars of Brown and McQueen's theoretical calculation, and $\sim$ 13% (740 K) less than the melting temperature reported for dynamic experiments which use diamond as the anvil material [Yoo et al., 1993], and 15% (900 K) greater than the melting temperature extrapolated from static compression data [Boehler, 1994]. Recent further exploration at high pressures and temperatures [Yoo et el., 1995; Yoo et al., 1997] suggest that our knowledge of the Fe phase diagram is incomplete, and as shown, a β phase of iron may be intersected by the Hugoniot curve at 243 $\pm$ 2 GPa, though the pressure range of the β phase is unknown.

3.6 Conclusions

For our experiments the anvil materials LiF and Al_2O_3 are shown to be transparent, using several lines of reasoning: First, There is a predictable systematic difference between Hugoniot temperatures of Fe and stainless steel. Second, there is no systematic dependence upon anvil material used for Hugoniot temperatures of Fe. Third, we observe a time dependence for emissivity, but no systematic time dependence for interface temperature during our "thin film" experiments. Fourth, due to the high shock pressures of our Fe films, $P_h > 190$ GPa, and due to the high temperatures caused by effective porosity in our "thin films" experiments, our "thin films" of Fe are expected to emit much more light than the "thick films" of Ag reported by Kondo for lower pressures, < 80 GPa. Thus, light from our films more easily overwhelms any light from the continuum thermal emission of the anvil media.

We successfully conducted "thin film" experiments to measure R. For Al_2O_3 values of 65 to 80 were obtained, as compared to LiF values of 15 to 35. For both anvil materials, observed values are equal within errors to the values calculated from Debye and electron gas theory, though the calculated values are in all cases slightly less than the observed values.

Experimental R values were used to revise iron Hugoniot temperatures. The revised shock temperatures do not show the expected offset in slope at the point that the Hugoniot intersects the fusion curve, so neither the shock pressure of the onset of melting, nor that of the completion of melting, is clearly obtained. However, a Hugoniot temperature of 5860 $\pm$ 390 K at the 243 $\pm$ 2 GPa, the pressure where sound speed measurements detect the onset of melting of iron.

3.7 Appendix - Thin film data analysis

Prior to each experiment, an optical radiance standard lamp (calibrated according to NIST standards at Optronics Laboratories) was placed in the position of the target. For experiments in which we expected intensities of $\leq 5 \times 10^{12}$ W/m^3, we used a 200 W standard lamp operating at 6.5 amps (model M416), and for shots in which we expected greater intensities, we used a 1000 W standard lamp operating at 8 amps (model OL200M). The radiance from the lamp was recorded as a voltage on the pyrometer's digitizing oscilloscopes (one channel for each wavelength) to be used as calibration data, $V_l(\lambda)$. The lamp was then removed and replaced with the target for the experiment.

The raw data for an experiment was recorded as voltage versus time, $V(\lambda, t)$ on the digitizing oscilloscopes. These digital data are cropped a hundred nanoseconds before and after the experiment so that only the times of interest are analyzed. Individual data points for a channel are deleted where the data went off scale. For two experiments (shots 285 and 297) an entire channel was not used because the data was off scale, leaving five usable channels. Calibration data, $V_l(\lambda)$, is used to calculate radiance, $I(\lambda, t)$ from voltage, $V(\lambda, t)$.

$$I(\lambda, t) = \frac{f_g I_l(\lambda)}{A\epsilon(\lambda)} \frac{V(\lambda, t)}{V_l(\lambda)} \ , \tag{3.12}$$

where $f_g = 2.5 \times 10^8$ m^2/Sr is a geometric factor, A is the area of the sample viewed by the pyrometer through the a mask (f_g/A represents the difference between the ex-

Table 3.4: Pyrometer calibration lamp radiance values, $I_l(\lambda)$, for the 200W and 1000 W spectral radiance standards operating at 6.5 and 8.0 amps respectively, and the emissivity of iron normalized to 1.0 [Touloukian, 1970]

Channel #	λ (nm)	$I_l(\lambda)$ 200W (10^{12}W/m^3)	$I_l(\lambda)$ 1000W (10^{12}W/m^3)	$\epsilon(\lambda)$ Fe (norm)
1	451.5	1.1390	5.090	0.992
2	555.5	2.6200	12.29	0.889
3	603.7	3.3046	16.78	0.845
4	661.5	4.0194	19.51	0.852
5	748.2	4.7890	23.71	0.878
6	904.0	4.9904	26.82	0.914

perimental target configuration and the lamp configuration when it was calibrated at Optronics Laboratories), and $I_l(\lambda)$ and $\epsilon(\lambda)$ are the calibration lamp standard intensities provided for each lamp by Optronics Laboratories, and the normalized wavelength dependence of emissivity for 1288 K, γ-iron [Touloukian, 1970] (Table 3.4).

Using least squares linear regression, the radiance data for the six channels are fit to the Planck function at each time to obtain temperature, $T(t)$ and emissivity, $\epsilon(t)$. If there is a systematic time dependence of ϵ, we assume the time dependence is seperable from the magnitude of the emissivity, $\epsilon(t) = \epsilon(t)_{\max}\epsilon(t)_{\text{normal}}$. To get $\epsilon(t)_{\text{normal}}$, we fit $\epsilon(t)$ to a polynomial, and normalize it so that the maximum value is one 1. We then divide all of the radiance data by $\epsilon(t)_{\text{normal}}$, effectively removing any observed systematic time dependence from the data. We then fit this corrected data to the Planck function to obtain a new $T(t)$ and $\epsilon(t)$ where the time dependence of ϵ has been normalized out, so the $\epsilon(t)$ function has no systematic time dependence although it may be quite noisy,

and the temperature decays with time (Figure 3.7). The fit has large error bars ($\sim$ 1000 K) and so the temperature decay can be fit to a wide range of slopes within the errors. However, the error bars on the decay of the radiance data are only 5% so we use the radiance curves to determine diffusivity ratio to greater accuracy than if we had just fit the temperature versus time curves. This procedure does not under-represent the errors in the fitting of the experiment, because the errors in the value of the initial temperature are taken into account when reporting the errors of deduced diffusivity ratio, R. The errors reported do, however, assume that noise in the $\epsilon(t)$ curves is random, rather than systematic. There is no specific theoretical reason to believe that there are any such systematic errors in $\epsilon(t)$, but if we incorporated their possibility into our error calculation, ΔR would increase by as much as 50%.

Using Equations A.11 and A.12 we scale the normalized results of the thermal decay model discussed in Chapter 5 of this thesis to the parameters of the experiment, using a calculated anvil temperature, T_a and the initial interface temperature T_i of the experiment, as determined by averaging the earliest five data points in the experiment after the initial rise in intensity. The temperature decay model is then scaled to the parameters of a specific pyrometer channel using the calibration data, $V_l(\lambda)$, and Equation 3.12. Figure 3.4 shows the model curves scaled to the parameters of pyrometer channel #3 for Shot 297; the experimental parameters are listed in Table 3.1.

The model curves are fit to a polynomial on log-log paper (R versus I), to facilitate interpolation between the model curve values (R=1, 10, 100 and 1000) of the experimental data to infer a value for R. An example of such an interpolation is given in Figure 3.8. This value of R is used to generate a new finite element model as discussed in Chapter 5, which is then scaled to the parameters of the experiment as discussed above and plotted as R=72 in Figures 3.7 and 3.4. In order to estimate the uncertainties for R given in Table 3.3, the entire procedure is repeated, scaling the finite element model curves to the highest and lowest values of T_i that fit the data. Equation 3.7 and

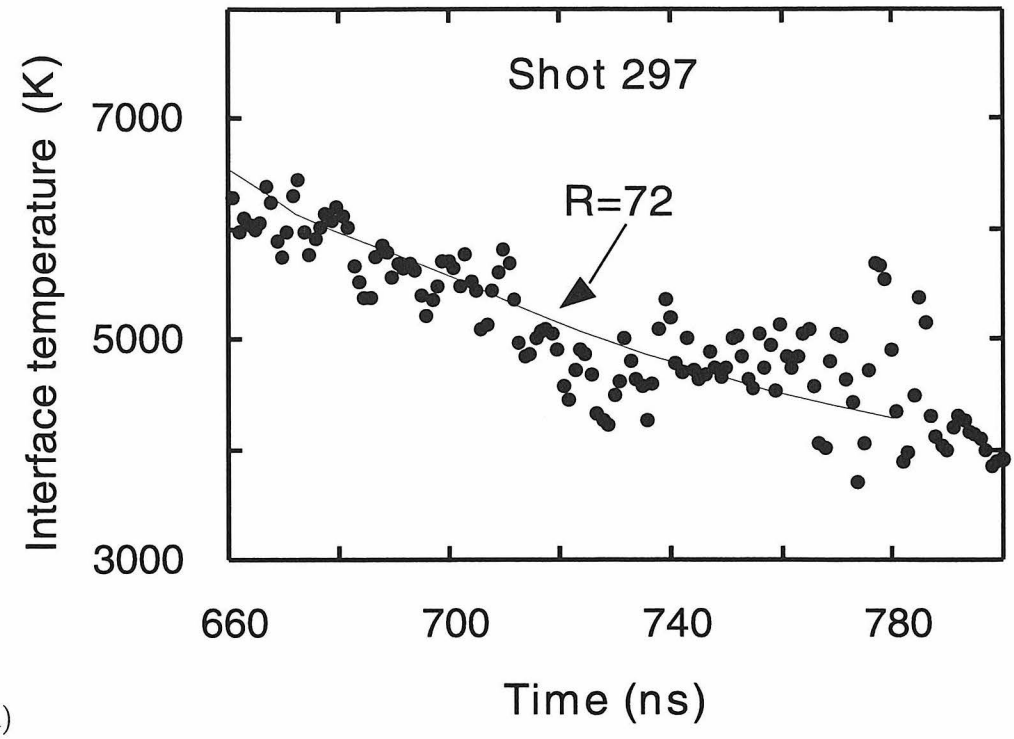

A)

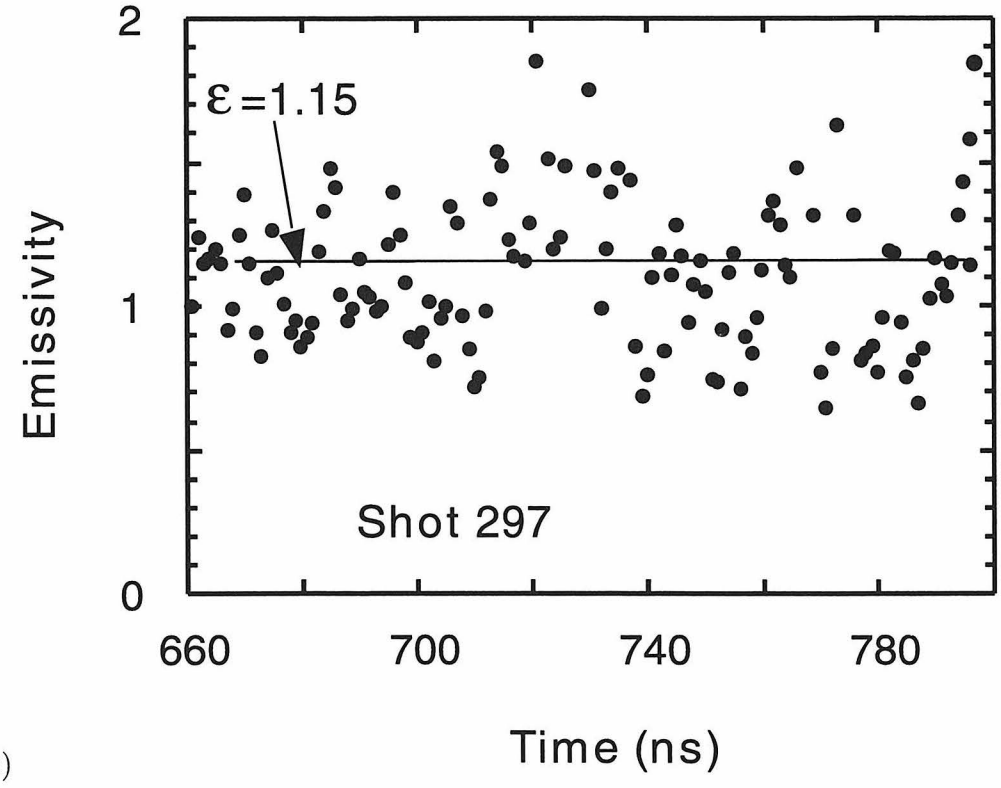

B)

Figure 3.7: Time dependent interface temperature A) and emissivity B) for Shot # 297, 1000 Å Fe with an Al_2O_3 anvil and driver. The solid curves are calculated from the best fit thermal diffusivity ratio R=72 and emissivity $\epsilon = 1.15$.

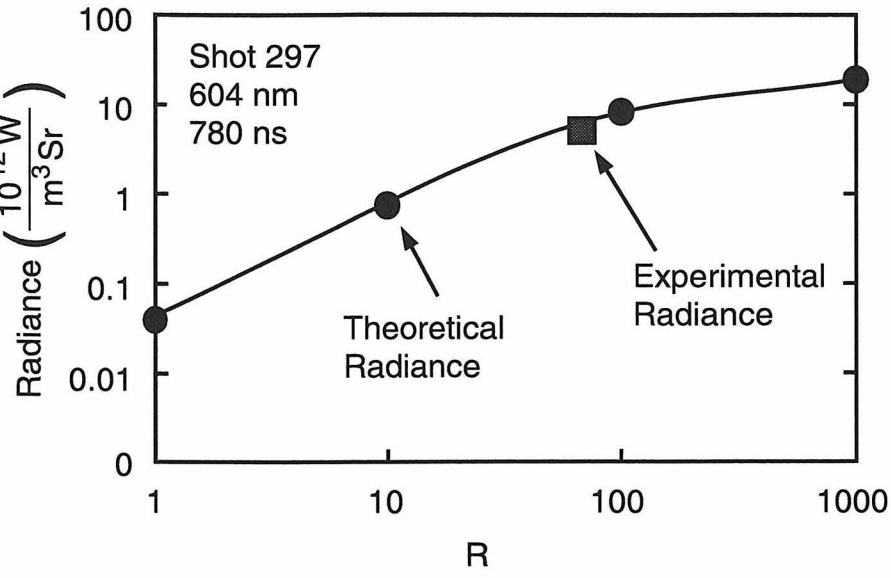

Figure 3.8: Interpolation between thermal diffusivity model curves R=1, 10, 100, 1000, scaled to the parameters of shot 297 at 604 nm and 780 ns. Solid circles indicate R values and scaled radiances of the four models. The solid square represents the radiance of the experiment shot 297 at the relevant time and wavelength, for which a value of $R = 75$ is being obtained. The interpolation is repeated for each of the 350 temporal data points and each of the six wavelength bands of the experiment, yielding a value for the experiment of 72±11.

the experimental uncertainty in R is then used to calculate a corresponding uncertainty in $\kappa_{T,P}$ for the anvil material, assuming that the uncertainty of $\kappa_{T,P}$ for the metal is much smaller that the uncertainty in the anvil material, because the value for the metal is calculated from electron gas theory.

Bibliography

Ahrens, T. J., G. Lyzenga, and A. C. Mitchell, Temperatures induced by shock waves in minerals: applications to geophysics, in *High-Pressure Research in Geophysics*, edited by S. Akimoto and M. H. Manghnani, pp. 579–594, Center for Acad. Pub., Tokyo, Japan, 1982.

Ahrens, T. J., Shock wave techniques for geophsyics and planetary physics, *Meth. of Exp. Phys., Vol. 24*, edited by C. L. Luke, pp. 185–235, Academic Press, New York, 1987.

Ahrens, T. J., H. Tan, and J. D. Bass, Analysis of shock temperature data for iron, *High Pressure Research - 1990*, 2, 145–157, 1990a.

Ahrens, T. J., J. D. Bass, and J. R. Abelson, Shock temperatures in metals, in *Shock Compression of Condensed Matter - 1989*, edited by S. C. Schmidt, J. N. Johnson, L. W. Davidson, pp. 851–857, Elsevier, Amsterdam, 1990b.

Ahrens, T. J., and M. L. Johnson, Shock wave data for minerals, In *A Handbook Of Physical Constants, Vol. 2*, Edited By T. J. Ahrens, pp. 143–184, Amer. Geophys. U., Washington, D. C., 1995.

Ahrens, T. J., Applications of shock compression science to Earth and planetary physics, in *Shock Compression of Condensed Matter*, edited by S. C. Schmidt and W. C. Tao, pp. 3–8, AIP Press, New York, 1996.

Allègre, C. J., J. P. Poirier, E. Humler, A. W. Hofmann, The chemical-composition of the Earth, *Earth Plan. Sci. Lett.*, 134, 515–526, 1995.

Bass, J. D., B. Svendsen, and T. J. Ahrens, The temperature of shock compressed iron, in *High Pressure Research In Mineral Physics* edited by M. H. Manghnani and Y. Syono, pp. 393–402, Terra Scientific, Washington, D. C., 1987.

Birch, F., Elasticity and constitution of the Earth's interior, *J. Geophys. Res.*, 57, 227–286, 1952.

Boehler, R., Melting of the Fe-FeO and the Fe-FeS systems at high-pressure – constraints on core temperatures, *Earth Planet. Sci. Lett.*, 111, 217–227, 1992.

Boehler, R., The phase diagram of iron to 2 Mbar: New static measurements, in *High-Pressure Science and Technology - 1993*, edited by S. C. Schmidt, J. W. Shaner, G. A. Samara, M. Ross, pp. 919–922, AIP Press, New York, 1994.

Boehler, R., M. Ross, and D. B. Boercker, High pressure melting curves of alkali-halides, *Phys. Rev. B*, 53, 556–563, 1996.

Boness, D. A., and J. M. Brown, Bulk superheating of solid KBr and CsBr with shock waves, *Phys. Rev. Lett.*, 71, 2931–2934, 1993.

Boslough, M. B., A model for the time-dependence in shock-induced thermal-radiation of light, *J. Appl. Phys.*, 58, 3394–3399, 1985.

Boslough, M. B., and T. J. Ahrens, A sensative time-resolved radiation pyrometer for shock temperature measurements above 1500 K, *Rev. Sci. Instr.*, 60, 3711–3716, 1989.

Bowen, N. L., and O. Anderson, The binary system MgO - SiO_2, *Am. Journ. Sci.*, 187, 487-500, 1914.

Brady, J. B., Diffusion data for silicate minerals, glasses and liquids, In *A Handbook Of Physical Constants, Vol. 2*, Edited By T. J. Ahrens, Pp. 269–290, Amer. Geophys. U., Washington, D. C., 1995.

Brown, J. M., and R. G. McQueen, Phase transitions, Grüneisen parameter, and elasticity for shocked iron between 77-GPA and 400-GPa, *J. Geophys. Res.*, 91, 4785–7494, 1986.

Brown, J. M., M. D. Furnish, D. A. Boness, Shock velocities for San Carlos Olivine, in *Shock Waves in Condensed Matter-1987*, edited by S. C. Schmidt and N. C. Holmes, pp. 119–122, Elsevier, New York, 1988.

Carslaw, H. S., and J. C. Jaeger, *Conduction of Heat in Solids. - 2nd Ed.* Oxford Science Publications, Clarendon Press, Oxford, 1959. Reprinted 1993.

Chen, G. High pressure melting of γ-iron and the thermal profile in the Earth's core, *Ph.D. thesis, California Institute of Technology*, Pasadena, CA, 1998.

Chen, M., T. G. Sharp, A. Elgoresy, B. Wopenka, and X. D. Xie, The majorite-pyrope plus megnesiowüstite assemblage - constraints on the history of shock veins in chondrites, *Science*, 271, 1570–1573, 1996.

Davis, L. S., and J. L. England, The melting of forsterite up to 50 kilobars, *J. Geophys. Res.*, 69, 1113–1116, 1964.

Duffy, T., and T. J. Ahrens, Thermal expansion of mantle and core materials at very high pressures, *Geophys. Res. Lett.*, 20, 1103–1106, 1993.

Dziewonski A. M., and D. A. Anderson, Preliminary reference earth model, *Phys. Earth. Planet. Inter.*, 25, 297–356, 1981.

Funamori, N., and R. Jeanloz, High-pressure transformation of Al_2O_3, *Science*, 278, 1109–1111, 1997.

Furnish, M. D., and J. M. Brown, Shock loading of single crystal olivine in the 100–200 GPa range, *J. Geophys. Res.*, 91, 4723–4729, 1986.

Gallagher, K. G., J. D. Bass, T. J. Ahrens, M. Fitzner, and J. R. Abelson, Shock temperature of stainless steel and a high pressure-high temperature constraint on thermal diffusivity of Al_2O_3, in *High-Pressure Science and Technology - 1993*, edited by S. C. Schmidt, J. W. Shaner, G. A. Samara and M. Ross, pp. 963–968, AIP Press, New York, 1994.

Gallagher, K. G., and T. J. Ahrens, Ultra-high-pressure thermal-conductivity measurements of griceite and corundum, in *Shock Waves, Vol. 2*, edited by B. Sturtevant, J. E. Shepherd and H. G. Hornung, pp. 1401–1406, World Scientific, Singapore, 1996.

Garnero, E. J., and D. V. Helmberger, A very slow basal layer underlying large-scale low-velocity anomalies in the lower mantle beneath the Pacific: evidence from core phases, *Phys. Earth Planet. Int.*, 91, 161–176, 1995.

Gasparik, T., Phase relations in the transition zone, *J. Geophys. Res.*, 95, 15, 751–769, 1990.

Greig, J. W., Immiscibility in silicate melts, *Amm. Journ. Sci.*, 213, 1–44, 1927.

Grover, R., and P. A. Urtiew, Thermal relaxation at interfaces following shock compression, *J. App. Phys.*, 45, 146–152, 1974.

Hashim, I., B. Park, and H. Atwater, Epitaxial growth of Cu (001) on Si (001): Mechanisms of orientation development and defect morphology, *Appl. Phys. Lett.*, 63, 2833–2835, 1993.

Heinz, D. L., E. Knittle, J. S. Sweeney, Q. Williams, and R. Jeanloz, High pressure melting of (Mg,Fe)SiO_3 perovskite, *Science*, 264, 279–280, 1994.

Hixon, R. S., R. G. McQueen, and J. N. Fritz, The shock Hugoniot of 316 SS and sound velocity measurements, in *High Pressure Science and Technology, 1993*, edited by S. C. Schmidt, J. W. Shaner, G. A. Samara and M. Ross, pp. 105–108, AIP Press, New York, 1994.

Hofmeister, A. M., Mantle values of thermal conductivity and the geotherm from phonon lifetimes, *Science*, 283, 1699–1706, 1999.

Holland, K. G., and T. J. Ahrens, Melting of $(Mg, Fe)_2SiO_4$ at the core-mantle boundary of the Earth, *Science*, 275, 1623–1625, 1997a.

Holland, K. G., and T. J. Ahrens, Properties of LiF and Al_2O_3 to 240 GPa for metal shock temperature measurements, in *High-Pressure-Temperature Research: Properties of Earth and Planetary Materials*, edited by M. Maghnani and T. Yagi, pp. 335 –343, Amer. Geophys. U., Washington, D. C., 1998.

Jeanloz, R., and T. J. Ahrens, Pyroxenes and olivines: structural implications of shock-wave data for high pressure phases, in High-Pressure Research: Applications in Geophysics, edited by M. Maghnani and S. Akimoto, pp. 439–461, Academic Press, San Diego, 1977

Jeanloz, R., and S. Morris, Temperature distribution in the crust and mantle, *Annu. Rev. Earth*, 14, 377–415, 1986.

Jephcoat, A., and P. Olson, Is the inner core of the earth pure iron?, *Nature*, 325, 332–335, 1987.

King, S. D., A. Raefsky, and B. H. Hager, ConMan: vectorizing a finite element code for incompressible two-dimensional convection in the earth's mantle, *Phys. Earth. Plan. Int.* 59, 195–207, 1990.

Knittle, E., and R. Jeanloz, Melting curve of (Mg,Fe)SiO_3 perovskite to 96 GPa: evidence for a structural transition in lower mantle melts, *Geophys. Res. Lett.*, 16, 421–424, 1989.

Kondo, K., and T. J. Ahrens, Heterogeneous shock-induced thermal radiation in minerals, *Phys. Chem. Min.*, 9, 173–181, 1983.

Kondo, K.-I., Window problem and complementary method for shock-temperature measurements of iron, in *High-Pressure Science and Technology - 1993*, edited by S. C. Schmidt, J. W. Shaner, G. A. Samara and M. Ross, pp. 1555–1558, AIP Press, New York, 1994.

Leibfried, G., and E. Schlömann, Wärmeleitung in elektrisch isolierenden kristallen. *Nachr. Akad. Wiss. Göttingen, Math Phys. Klasse I A*, 4, 71–152, 1954.

Lyzenga, G. A., and T. J. Ahrens, Shock temperature measurements in Mg_2SiO_4 and SiO_2 at high pressures, *Geophys. Res. Lett.*, 7, 141–144, 1980.

Lyzenga, G., Shock temperatures of materials: experiments and applications to the high pressure equation of state, *Ph.D. thesis, California Institute of Technology*, Pasadena, CA, 1982.

Lyzenga, G. A., T. J. Ahrens, and A. C. Mitchell, Shock temperatures of SiO_2 and their geophysical implications, *J. Geophys. Res.*, 88, 2431–2444, 1983.

Madon, M., and J. P. Poirier, Transmission elecron microscope observation of α, β, and γ $(Mg,Fe)_2SiO_4$ in shocked meterorites: planar defects and polymorphic transitions, *Phys. Earth Planet. Int.*, 33, 31–44, 1983.

Manga, M., and R. Jeanloz, Implications of a metal-bearing chemical boundary layer in D" for mantle dynamics, *Geophys. Res. Lett.*, 23, 3091–3094, 1996.

Manga, M., and R. Jeanloz, Thermal conductivity of corundum and periclase and implications for the lower mantle, *J. Geophys. Res.*, 102, 2999–3008, 1997.

Mao, H. K., and P. M. Bell, Electrical conductivity and the red shift of absorption in olivine and spinel at high pressures, *Science*, 176, 403–406, 1972.

Mao, H. K., Observations of optical absorption and electrical conductivity in magnesiowüstite at high pressures, *Carnegie Inst. of Wash. Yearbook*, 72, 554–557, 1973.

Matassov, G., The electrical conductivity of iron-silicon alloys at high pressures and the Earth's core, *Ph.D. Thesis, University of California, Livermore*, Chapter 7, 1977.

Marsh, S. P. (Ed.), *LASL Shock Hugoniot Data*, 658 pp., University of California Press, Berkeley, 1980.

McQueen, R. G, S. P. Marsh, and J. N. Fritz, Hugoniot equation of state of twelve rocks, *J. Geophys. Res.*, 72, 4999-5036, 1967.

McQueen, R. G., S. P. Marsh, J. W. Taylor, J. N. Fritz, and W. J. Carter, The equation of state of solids from shock wave studies, in *High Velocity Impact Phenomena*, edited by R. Kinslow, pp. 294–419, Academic Press, New York, 1970.

McQueen, R. G., and D. G. Isaak, Characterizing windows for shock wave radiation studies, *J. Geophys. Res.*, 95, 21753–21765, 1990.

Nellis, W. J., and C. S. Yoo, Issues concerning shock temperature measurements of iron and other metals, *J. Geophys. Res.*, 95, 21749–21752, 1990.

Pedrotti, F. L., and L. S. Pedrotti, *Introduction to optics*, Prentice-Hall, New Jersey, 1987.

Presnall, M. J. and D. C. Walter, Melting of forsterite, Mg_2SiO_4, from 9.7 to 16.5 GPa, *J. Geophys. Res.*, 98, 19777-19783, 1993.

Presnall, D. C., Phase diagrams of Earth forming materials, in *A Handbook of Physical Constants, Vol. 2*, edited by T. J. Ahrens, pp. 248–268, Amer. Geophys. U., Washington, D. C., 1995.

Roufosse, M. C., and R. Jeanloz, Thermal conductivity of minerals at high pressure: the effect of phase transitions, *J. Geophys. Res.* 88, 7399–7405, 1983.

Secco, R. A., and H. H. Schloessin, The electrical-resistivity of solid and liquid Fe at pressures up to 7 GPa, *J. Geophys. Res.*, 94, 5887–5894, 1989.

Shen, G. Y., and P. Lazor, Measurement of melting temperatures of some minerals under lower mantle pressures, *J. Geophys. Res.*, 100, 17699–17713, 1995.

Stixrude, L., R. J. Hemley, Y. Fei, and H. K. Mao, Thermoelasticity of silicate perovskite and magnesiowustite and stratification of the Earth's mantle, *Science*, 257, 1099–1101, 1992.

Svendsen, R. F., J. D. Bass, and T. J. Ahrens, Optical radiation from shock compressed materials and interfaces, *Phys. Rep.*, 180, 333–416, 1989a.

Swartz, E. T., and R. O. Pohl, Thermal boundary resistance, *Rev. Mod. Phys*, 61, 605–668, 1989.

Sweeney, J. S., and D. L. Heinz, Irreversible melting of a magnesuim-iron-silicate perovskite at lower mantle pressures, in High-Pressure-Temperature Research: Properties of Earth and Planetary Material, edited by M. Manghnani and Y. Syono, in press, Amer. Geophys. U., Washington, D. C., 1997.

Syono, Y., T. Goto, H. Takei, M. Tolonami, and K. Nobugai, Dissociation reaction in forsterite under shock compression, *Science*, 214, 177, 1981.

Tan, H., and T. J. Ahrens, Shock temperature measurements for metals, *High Pressure Research*, 2, 159–181, 1990.

Tang, W., The pressure and temperature dependence of thermal conductivity for non-metal crystals, *Chinese J. High Press. Phys.*, 8, 125, 1994.

Tang, W., F. Jing, R. Zhang, and J. Hu, Thermal relaxation phenomena across the metal/window interface and its significance to shock temperature measurements of metals, *J. Appl. Phys.*, 80, 3248–3253, 1996.

Touloukian, Y. S., Normal spectral emittance of iron, in *Thermophysical properties of matter. [The TPRC data series; a comprehensive compilation of data], Vol. 1*, edited by Y. S. Touloukian, pp. 316–318, Plenum, New York, 1970.

Urtiew, P. A., and R. Grover, Temperature deposition caused by shock interactions with material interfaces, *J. App. Phys.*, 45, 140–145, 1974.

Weidner, D. J., Mantle model based on measured physical properties of minerals, in *Chemistry and Physics of Terrestrial Planets, chapter 7*, edited by S. K. Saxena, pp. 251–274, Springer-Verlag, New York, 1986.

Williams, Q., R. Jeanloz, J. D. Bass, B. Svendson, and T. J. Ahrens, Melting curve of iron to 250 GPa: a constraint on the temperature of the Earth's center, *Science*, 236, 181–182, 1987.

Williams, Q., and E. J. Garnero, Seismic evidence for partial melting at the base of the mantle, *Science*, 273, 1528–1530, 1996.

Yang, W., Impact volatilization of calcite and anhydrite and the effect on global climate from K/T impact crater at Chicxulub, *Ph.D. thesis, California Institute of Technology*, Chapter 4, Pasadena, CA, 1996.

Yoo, C. S., N. C. Holmes, M. Ross, D. J. Webb, and C. Pike, Shock temperatures and melting of iron at Earth core conditions, *Phys. Rev. Lett.*, 70, 3931–3934, 1993.

Yoo, C. S., J. Akella, A. J. Campbell, H. K. Mao, and R. J. Hemley, Phase-diagram of iron by in-situ x-ray-diffraction - implications for earth's core, *Science*, 270, 1473–1475, 1995.

Yoo, C. S., A. J. Campbell, H. K. Mao, and R. J. Hemley, Detecting phases of iron - Response, *Science*, 275, 96–96, 1997.

Zerr, A., and R. Boehler, Melting of (Mg,Fe)SiO_3-perovskite to 625 kilobars: indication of a high melting temperature in the lower mantle, *Science*, 262, 553–555, 1993.

Zerr, A., and R. Boehler, Constraints on the melting temperature of the lower mantle form high-pressure experiments on MgO and magnesiowüstite, *Nature*, 371, 506–508, 1994.

Appendix A

Thermal Diffusion Calculations for Sandwich Configuration Shock Temperature Experiments

A.1 Introduction

The experimental determination of shock temperatures in metals of geophysical interest, such as iron, is conducted by sandwiching a metal film between a transparent anvil, such as LiF, Al_2O_3 or C (diamond), and a driver plate. The driver plate can be made of iron, or of the same material as the anvil. We discuss here the latter case.

A strong shock is driven through the driver into the film, heating it to temperatures in the range of 4000 - 10000 K, so that it emits thermal radiation in the optical range. Using near-infrared and optical pyrometery, the spectral radiation is recorded. This radiation is emitted from an interface between the desired metal sample and the anvil material, which is usually at a lower shock temperature than the metal. For the case where the driver and the metal sample are the same material, the correction from

the observed interface temperature to the Hugoniot shock temperature of the metal is dependent on the ratio of the thermal diffusivities of the two materials [Grover and Urtiew, 1974]. The case where the driver material is the same as the anvil material does not have a simple analytic solution and is treated in detail here. Previously, the thermal diffusivities of the anvils that were used were constrained only to first order by Debye theory [Bass et al., 1987; Ahrens et al., 1990b]. The applicability of Debye theory, as developed by Roufosse and Jeanloz [1983] and reviewed in Section 3.2 of this thesis is largely untested and comparisons between theory and experiment are scarce [Manga and Jeanloz, 1997]. Recently, Hofmeister [1999] developed a more detailed theory which considers phonon lifetimes and transport due to blackbody radiation as well as lattice vibrations in predicting the temperature and pressure dependence of thermal conductivities of insulating materials. While Hofmeister's theory shows promise, and may do a better job than previous theories, it is largely untested. Therefore a series of experiments were conducted to measure the high pressure diffusivities of the anvil materials during shock experiments which employed a thin metal film sandwiched between two pieces of an anvil material. Thus a theoretical understanding of the time dependent thermal behavior of dissimilar materials in the sandwich configuration of our experiments is of interest.

In this appendix of this thesis, we review the relevant experimental configuration. Then we describe an approximate analytic model which describes heat flow in the target, but which assumes that the metal is at a higher temperature than the anvil and that the thermal diffusivity, κ, is the same in the metal and in the anvil. We also discuss another approximate model which uses differing thermal diffusivities, but assumes that both the metal and anvil are thick enough so that they may be considered infinitely thick. Finally, we discuss a more accurate model, which was calculated with the aid of a finite element code [King et al., 1990]. The finite element code is first compared to the analytical models, and then used to model our experiments.

A.2 Review of experimental methods

the present paper A metal film of $\sim$ 500 Å to 1 μm thickness was sandwiched between two pieces of single crystal Al_2O_3 or LiF of 2 – 4 mm thickness. A shock wave is passed through the composite sample so that each material will be approximately at its peak shock temperature initially, because the time-scale on which the shock wave propagates is much less than the time-scale of cooling by diffusion. The initial shock temperature of the metal, T_m, is generally a few thousand degrees Kelvin above the temperature of the anvil, T_a, although its shock pressure is usually lower than the peak pressure achieved in the metal because of multiple unloading waves, such that the pressure in the metal film becomes equilibrated with the pressure in the anvil. Thus the initial pressures are equal but the temperature distribution is a boxcar function. During the $\sim$ 300 ns of the experiment, heat flows from the high temperature metal into the relatively low temperature anvil, with the axis of symmetry at the center plane of the metal film. The metal/anvil interface temperature decreases with time. This decrease is a function of the ratio of thermal diffusivities, $R = \kappa_m/\kappa_a$, between the metal and the anvil material at the high temperature and pressure conditions of those materials.

Figure A.1 shows a sketch of the expected temperatures seen with time in shock temperature experiments. For transparent materials, a constant temperature with time is expected during the time the shock wave travels through the sample. However, for the above described thin film experiment on metal samples with transparent dielectric anvils, a decreasing temperature is expected with time.

A.3 Calculations

To quantify the decrease in temperature expected for the above described experiment, we model the one-dimensional heat flow between two parallel planes. The thermal

conduction equations relevant to heat flow in the "sandwich" type configuration are

$$\frac{\delta^2 T_m}{\delta x^2} - \frac{1}{\kappa_m}\frac{\delta T_m}{\delta t} = 0,\ x \leq a \tag{A.1}$$

$$\frac{\delta^2 T_a}{\delta x^2} - \frac{1}{\kappa_a}\frac{\delta T_a}{\delta t} = 0,\ x > a \tag{A.2}$$

Here, T_m and T_a are the temperatures in the metal and in the anvil, κ_m and κ_a are the thermal diffusivities in the metal and anvil, x is the position in the target relative to the axis of symmetry that coincides with the center plane of the metal, and a is half the thickness of the sample. Equations A.1 and A.2 are the one-dimensional heat

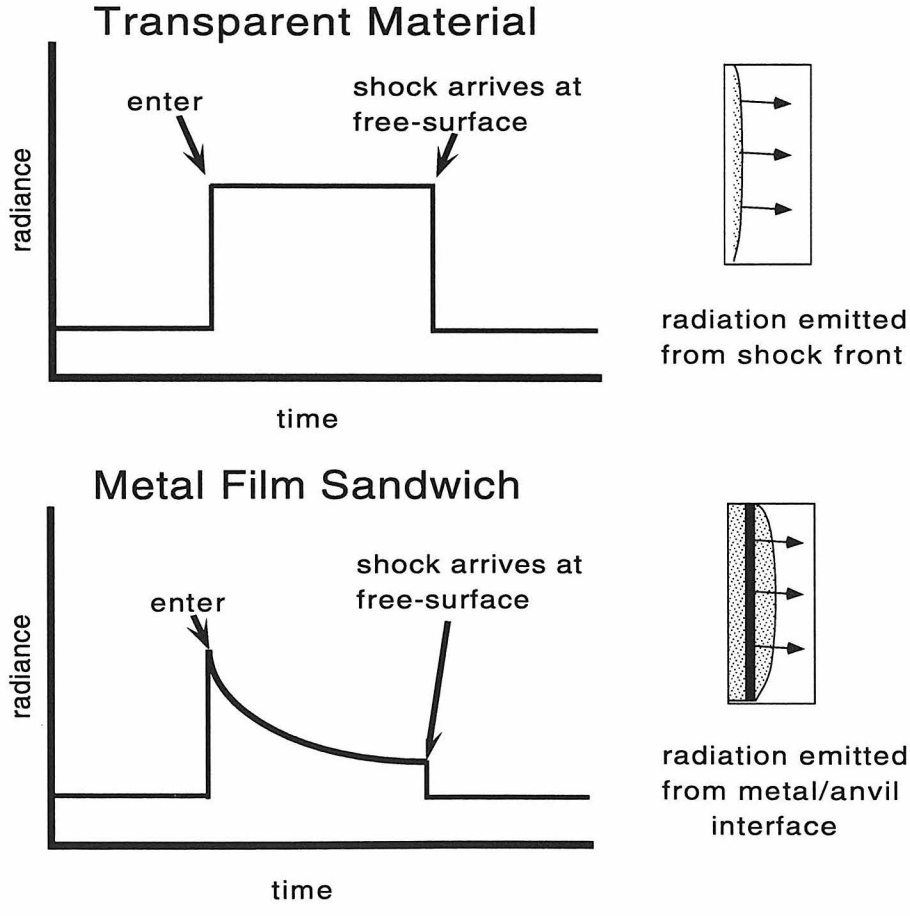

Figure A.1: Sketch of radiance versus time for shock temperature experiments. For a transparent sample, a constant temperature is seen while the shock wave propagates through the sample. For a "thin film" experiment, the metal/anvil interface temperature decreases with time.

flow equations [Carslaw and Jaeger, 1993]. The initial conditions and thermal boundary conditions are:

$$T_m(t = 0, x \leq a) = T_R \tag{A.3}$$

$$T_a(t = 0, x > a) = 0 \tag{A.4}$$

$$T_a(t, x = \infty) = 0 \tag{A.5}$$

$$\frac{\delta T_a}{\delta x} = 0,\ x = 0 \tag{A.6}$$

Here t is time since heat flow began and T_R is the release shock temperature of the metal. Analytic solutions of the above thermal conduction equations for certain end-member cases can be derived. When $\kappa_m/\kappa_a = 1$, the analytic solution [Carslaw and Jaeger, 1993, page 54] is:

$$T = \frac{T_R}{2}\left\{\mathrm{erf}\left(\frac{a-x}{2\sqrt{\kappa t}}\right) + \mathrm{erf}\left(\frac{a+x}{2\sqrt{\kappa t}}\right)\right\}\ , \tag{A.7}$$

where $\kappa \equiv \kappa_m \equiv \kappa_a$. Since the anvil material has a lower conductivity than the metal, conduction into the anvil limits in the flow of heat. Thus if we assume κ is equal to the value of κ_a, then we can use Equation A.7 to provide an upper bound to the correct solution.

Additionally, at early times when the heat diffusing from the metal into the anvil has not progressed far enough such that the temperature at the center of the metal (the plane of symmetry of the calculation) has not been perturbed, then the metal acts as an infinite half-space. The solution to the temperature profiles within two infinite half-spaces, in ideal contact, with differing diffusivities [Carslaw and Jaeger, 1993, page 88] is:

$$T_m = \frac{k_m \kappa_m^{-\frac{1}{2}} T_h}{k_m \kappa_m^{-\frac{1}{2}} + k_a \kappa_a^{\frac{1}{2}}}\left\{1 + \frac{k_a \kappa_a^{-\frac{1}{2}}}{k_m \kappa_m^{-\frac{1}{2}}}\mathrm{erf}\left(\frac{x}{2\sqrt{\kappa_m t}}\right)\right\} \tag{A.8}$$

$$T_a = \frac{k_m \kappa_m^{-\frac{1}{2}} T_h}{k_m \kappa_m^{-\frac{1}{2}} + k_a \kappa_a^{\frac{1}{2}}} \mathrm{erfc}\left(\frac{|x|}{2\sqrt{\kappa_m t}}\right) , \tag{A.9}$$

where the subscripts "a" and "m" represent the anvil and metal respectively and $k = \kappa\rho C_p$ is the thermal conductivity of the anvil.

For stainless steel, a film ~ 10 μm in thickness is sufficient for this assumption to be valid [Chapter 2 of this thesis]. The analytic model for thick films predicts that as heat flows across the interface, the interface temperature will not change. This is the reason we must use such thin films (~ 500 Å in thickness) in order to measure diffusivities.

In order to accurately model later times, a finite element calculation was performed using the "ConMan" Software package. The input files for a sample run are included in Figures A.2 and A.3. There were 2×100 cells in the calculation, so there were 303 corners. The first 2×10 cells correspond to the half-thickness of the metal film, and the last 2×90 cells correspond to the anvil. Distances, temperatures and times were all non-dimensional as follows:

$$x = \frac{\text{distance}}{a} \times 3.4 \tag{A.10}$$

$$T = \frac{\text{temperature} - T_a}{T_R - T_a} \tag{A.11}$$

$$t = \frac{\kappa_m}{a^2} \times \text{time} \tag{A.12}$$

where a is half the thickness of the film, T_R is the initial (release) temperature in the metal, T_a is the initial temperature in the anvil, and κ_m is the thermal diffusivity of the metal. The value 3.4 in equation A.10 comes from the fact that we used 100 cells, and the first 34 cells represented the metal while the last 66 represented the anvil. The initial non-dimensional temperature was 1 for the metal cells and 0 for the anvil cells. The normalized diffusivity was 1 for the metal cells and 1.0, 0.1, 0.01, and 0.001 for the anvil cells in our four calculations, respectively. There was no heat flow at the center, and the 100th cell was held at zero temperature. Due to the fact that the calculations showed

```
100 by 2 element input deck for a heterogeneous conduction problem
303 2 2 100 2 2 1 1 1 1 202 0 1 1 1 0
5000 2 0.5 0.0005 0.000001
5000 5000 500 500
1 301 3    0 1
301 303 1  1 1
1 3 1      1 1
3 303 3    1 1
1  1 1     1 1
3  3 1     1 1
301 301 1  1 1
303 303 1  1 1
0 0 0   0 0
301 303 1 1
0 0 0   0
1 301 3
3 303 3
0 0 0
2 302 3
2 302 3
0 0 0
0.001 1.0 1.0
2 200 4 4 2 2 0 5 0 0
1.0      1.0
1.0e07   1.0e07
1.0      1.0
10.0     10.0
0.0      0.0
0.0      0.0
0.0      0.0
```

Figure A.2: The main "i" input file for ConMan for the case $\kappa_m/\kappa_a = 1$.

```
1 4 0.0 0.0
301 1 10.0 0.0
303 1 10.0 0.2
3 1 0.0 0.2
100 3 2 1
0 0 0.0 0.0
0 0 0.0 0.0
301 0 0.0
302 0 0.0
303 0 0.0
0 0 0.0 0.0
1 1 1 1 4 5 2
100 2 3 2 1 1
21 1 2 31 34 35 32
90 2 3 2 1 1
0 0 0 0 0 0 0
```

Figure A.3: The supplemental "g" input file for ConMan, for the case $\kappa_m/\kappa_a = 1$.

that the temperatures in the the T=5 and T=25 cases were perturbed at x=9 for the later times, the T=5 and T=25 cases were calculated with 200 and 500 cells respectively, with only the first 100 cells being plotted in the figure for direct comparison with the other cases. This does not effect the normalization because the metal is still represented by the first 34 cells.

For many of our experiments, the initial shock temperature of the metal is hot enough so the film will be molten. As the metal film cools via conduction of heat into the anvil, it should undergo a phase change into solid iron. The latent heat of this phase change has not been taken into account in this calculation. Additionally, the thermal diffusivity in the finite element calculation is not temperature dependent. Further study would be required to incorporate latent heat or the temperature dependence of thermal diffusivity into this calculation. We have not determined the importance of these two approximations. The effect of not taking into account the latent heat of freezing would

be an over-prediction of the interface temperature, and the effect of not using temperature dependent diffusivities would be to under-predict the interface temperatures, at later times. A temperature-dependent diffusivity model would produce higher curvature in the theoretical interface versus time plane.

In order to verify that we performed our finite element calculations correctly, the results of the finite element calculations were compared with analytic solutions of the above thermal conduction equations for certain end-member cases. Figure A.4 compares the results of the finite element model for the case where $\kappa_m/\kappa_a = 1$ with the analytic model for that same condition. Note that the finite element model produces the same overall shape as the analytic model Equation A.7 and that the interface temperatures predicted with the finite element model are within 3% of those predicted with the

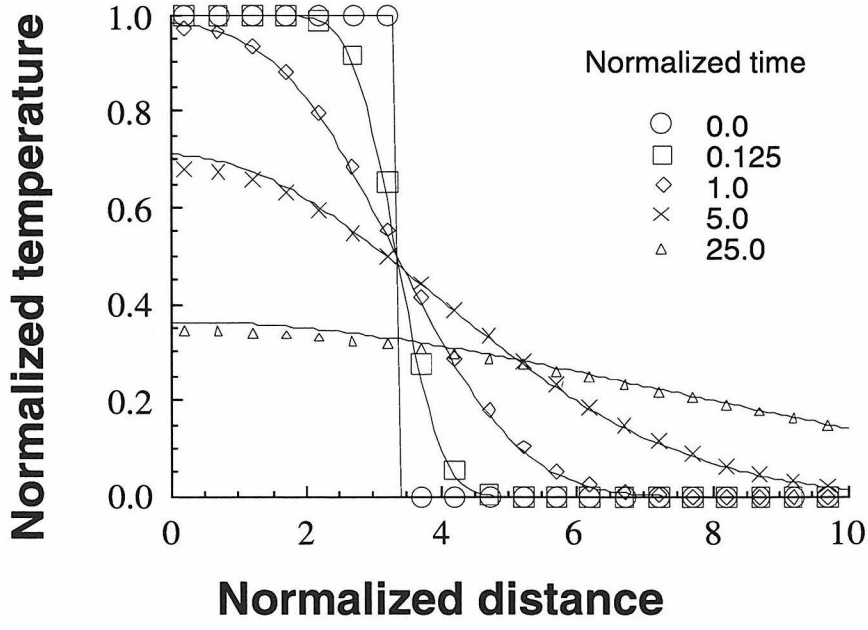

Figure A.4: Comparison of analytic (Equation A.7) and finite element (ConMan) solutions for the case $\kappa_m/\kappa_a = 1$. Normalized times are $t = 0$, 0.125, 1.0, 5.0 and 25.0 for the circles, squares, diamonds, exes and triangles respectively. Normalizations are defined in Equations A.10 through A.12.

analytic model. The temperatures at the axis of symmetry are within 6% of those predicted with the analytic model. Since the measurement errors of the temperatures in the experiments are 300 to 400 K (7 to 8%) the 6% agreement between the analytic and finite difference calculations is acceptable. By refining the mesh, one should be able to make the calculation more accurate, if necessitated by the experiments becoming more precise.

Figure A.5 compares the thin film finite element model for the case $\kappa_m/\kappa_a = 10$ with the infinite half-space analytic model Equations A.8 and A.9 for the same diffusivity ratio. As is expected, the models agree at early times but diverge at later times, when

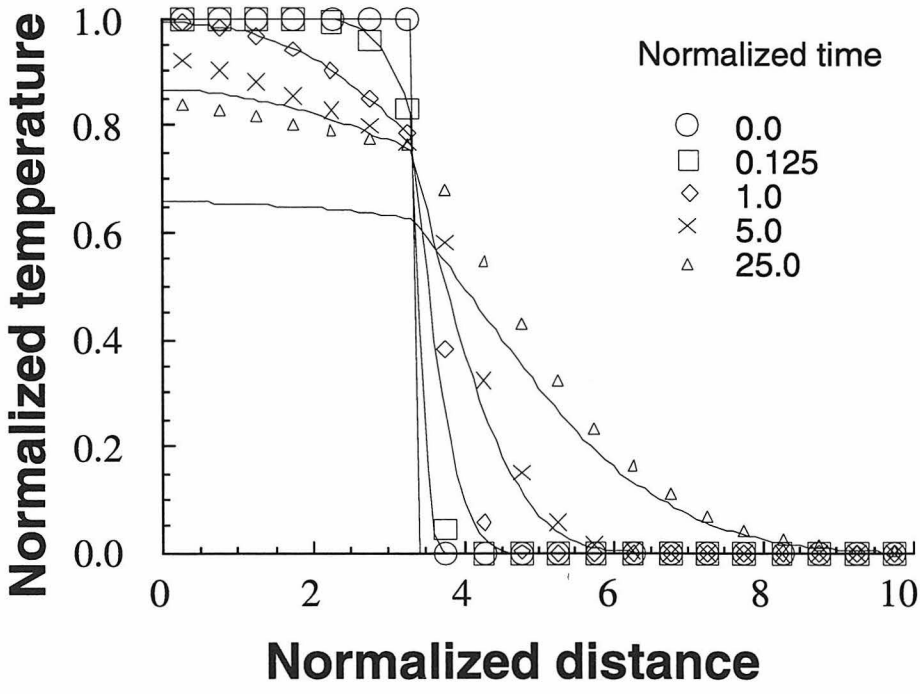

Figure A.5: Comparison of the analytic (Equations A.8 and A.9) and finite element (ConMan) solutions for the case $\kappa_m/\kappa_a = 10$. The parameters are the same as in figure A.4. Note that since the analytic solution makes the assumption that the metal is an infinite half-space, but ConMan solution is calculated for a metal with a finite thickness, the solutions diverge at later times. Normalizations are defined in Equations A.10 through A.12.

the thermal diffusion length-scale achieves a value comparable to that of the thickness of the film. Note that for the later time-steps, the analytic and finite element solutions agree for $x \gg a$ but that the interface temperatures disagree. Figures A.4 and A.5 show that the "ConMan" software is behaving in the way it is expected to, and that the obtained solutions are believable.

A.4 Results

Figure A.6 shows the finite element results for all four cases, $\kappa_m/\kappa_a = 1$, 10, 100 and 1000. As R gets higher, the interface temperature is closer to the shock temperature of the metal. Thus, underestimating R leads to overly estimating the upward temperature correction from T_i to T_h. Our experiments are consistent with a values of R of 15 – 80, while Equation 3.6 predicts R between 11 and 60 (see Table 3.3), so previous calculations

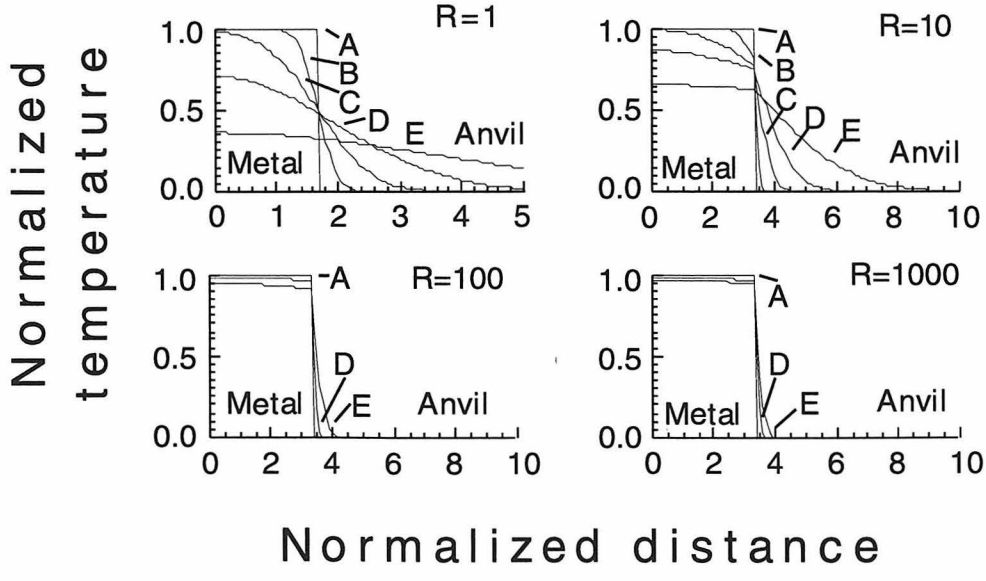

Figure A.6: Comparison of the numerical models for diffusivity ratios of R = 1, 10, 100 and 1000. The curves labeled A, B, C, D and E represent temperature profiles for dimensionless times of 0.0, 0.125, 1.0, 5.0, and 25.0, respectively. Note that as R gets higher, the interface temperature is closer to the shock temperature of the metal. Normalizations are defined in Equations A.10 through A.12.

have underestimated κ_a by a factor of ~ 2, and therefore overestimated T_h by about 350 K.